Juliane Dannberg, Zachary Eilon, Joshua B. Russell, and Rene Gassmöller contributed equally to this work.

Key Points:

- 3D models with complex rheology and evolving grain size require low asthenospheric viscosity to match observed SSC in the central Pacific
- In our models, the seafloor depth–age curve flattens at a plate age (∼60 Ma) matching global observations, despite young SSC onset (∼35 Ma)
- A small amount of melt and volatiles is required to match the observed asthenospheric low seismic velocities and high attenuation

Author Contributions:

Conceptualization: Juliane Dannberg, Zachary Eilon, Joshua B. Russell, Rene Gassmöller
Formal analysis: Juliane Dannberg, Zachary Eilon, Joshua B. Russell, Rene Gassmöller
Investigation: Juliane Dannberg, Zachary Eilon, Joshua B. Russell, Rene Gassmöller

Understanding Sub-Lithospheric Small-Scale Convection by Linking Models of Grain Size Evolution, Mantle Convection, and Seismic Tomography

Juliane Dannberg[1], Zachary Eilon[2], Joshua B. Russell[3], and Rene Gassmöller[1]

[1]GEOMAR Helmholtz Centre for Ocean Research Kiel, Kiel, Germany, [2]Department of Earth Science, UC Santa Barbara, Santa Barbara, CA, USA, [3]Department of Earth and Environmental Sciences, Syracuse University, Syracuse, NY, USA

Abstract The interaction between aging oceanic plates and their underlying mantle is a crucial component of the plate tectonic cycle. Sub-lithospheric small-scale convection (SSC) explains why plates appear not to thicken after a certain age. Here, we link grain-scale processes, dynamic models of asthenospheric flow, and seismic observations to gain new insights into the mechanisms of SSC. We present high-resolution 3D geodynamic models of oceanic plate evolution with an Earth-like rheology including coupled diffusion/dislocation creep and their interplay with evolving olivine grain size. Our models quantify how rheology affects the morphology and temporal stability of SSC, and we directly relate these quantities to geophysical observations from the Pacific OBS Research into Convecting Asthenosphere (ORCA) experiment. We convert variations in temperature, pressure, grain size, water content and stable melt fraction to seismic velocity and attenuation, seeking to match the wavelength and pattern of observed longitudinal convective rolls, the young SSC onset age, the large seismic velocity heterogeneity, low absolute seismic velocities, and high seismic attenuation. This requires low ($<2 \times 10^{19}$ Pa s) asthenospheric viscosity, the contribution of both diffusion and dislocation creep to deformation, and the presence of volatiles and melt. Although SSC occurs at plate ages ≪60 Ma in our best-fit model, the plate thermal structure approximately matches global observations of heat flux and bathymetry, indicating an important role of vigorous SSC in Earth's plate dynamics. However, reconciling all seismological observations is challenging, and additional mechanisms are required to explain the strong velocity heterogeneities suggested by body wave tomography.

Plain Language Summary As oceanic tectonic plates age, they get colder and thicker. At some point, portions of the base of the plates may drip off into the hot mantle underneath them, a process known as "small-scale convection" (SSC). This might explain diverse geophysical observations, including seismic imaging of cold blobs beneath the plates and the finding that plates seem to stop cooling with increasing age after they turn ∼70 million years old. We conducted computer simulations of aging oceanic plates that include novel components, such as more complex treatment of viscosity and its interplay with the size of crystal grains in rocks. Grain size turns out to be a key parameter in determining both how cold drips evolve and how seismic waves propagate through those rocks, which is how we identify structures beneath the surface. We link together the computer simulations with seismological studies by using simulated structure to predict synthetic earthquake data, for comparison with observations. In particular, we seek to match various attributes of apparent SSC seen recently beneath the central Pacific ocean plate. We find that small-scale convection is indeed reproduced by our simulations, and determine that it manifests in a way that is consistent with several real-Earth observations.

1. Introduction

Small-scale convection (SSC) at the base of oceanic lithosphere has been proposed as a key process for mediating the thermal evolution of the plates, redistributing mass and heat, and explaining the canonical departure of seafloor depth and heatflow observations from half-space cooling predictions (Buck & Parmentier, 1986; Crosby et al., 2006; Huang & Zhong, 2005; Ma & Dalton, 2019; Parmentier, 2015; Parsons & Sclater, 1977; Richter, 1973; Stein & Stein, 1992). Additionally, this process may explain mid-plate gravity undulations (Buck, 1986; Haxby & Weissel, 1986; Marquart et al., 1999), off-axis non-hotspot volcanism (Ballmer et al., 2007, 2009), and intraplate melting (e.g., Harmon et al., 2011). The feasibility and extent of SSC beneath the plates depends on asthenospheric temperature and rheology (Huang & Zhong, 2005; Huang et al., 2003; Marquart, 2001; Sleep, 2011; Van Hunen

Methodology: Juliane Dannberg,
Zachary Eilon, Joshua B. Russell,
Rene Gassmöller
Software: Juliane Dannberg,
Zachary Eilon, Joshua B. Russell,
Rene Gassmöller
Validation: Juliane Dannberg,
Zachary Eilon, Joshua B. Russell,
Rene Gassmöller
Visualization: Juliane Dannberg,
Zachary Eilon, Joshua B. Russell,
Rene Gassmöller
Writing – original draft:
Juliane Dannberg, Zachary Eilon, Joshua
B. Russell, Rene Gassmöller
Writing – review & editing:
Juliane Dannberg, Zachary Eilon, Joshua
B. Russell, Rene Gassmöller

et al., 2005); accurately describing the latter requires a sophisticated incorporation of the effects of grain size (Dannberg et al., 2017; Hall & Parmentier, 2003).

1.1. Evidence for SSC Beneath the Plates

Until recently, arguments regarding uppermost mantle convection have relied on proxy observations, often at the scale of entire ocean basins. Seismological evidence for this process has been absent or indirect: apparently disrupted sub-plate shear (Lin et al., 2016; van Hunen & Čadek, 2009), ridge-adjacent velocity perturbations (Weeraratne et al., 2007), or large-scale (>2,000 km wavelength) velocity variations in global models (French et al., 2013). However, high-resolution observations of uppermost oceanic mantle obtained through focused ocean-bottom seismometer (OBS) deployments have provided new perspectives on the prevalence and character of this oceanic SSC. Near the mid-Atlantic ridge, surface wave data reveal a possible lithospheric drip beneath ~32 Ma lithosphere (Harmon et al., 2020). In the Pacific, surprisingly large V_P variations of as much as 8% were observed in the asthenosphere beneath 160–180 Ma seafloor, and attributed to plume activity or SSC (H. Kang et al., 2023).

The Pacific OBS Research into Convecting Asthenosphere (ORCA) experiment (Eilon, Gaherty, et al., 2022) was designed to investigate the cause of prominent gravity undulations in the mid-Pacific by imaging oceanic asthenosphere. Two 30-instrument arrays of broadband seismometers were deployed for ~13 months on 40–45 Ma seafloor ("Young ORCA") and 84–92 Ma seafloor ("Old ORCA"). Teleseismic body-wave tomography beneath the Young ORCA region (Eilon, Zhang, et al., 2022) revealed substantial velocity variations, up to ±2% in V_P, arranged in alternating longitudinal cylinders with horizontal wavelength of ~250 km. The strongest lateral velocity heterogeneity was not found at the base of the plate (~70 km, assuming standard cooling) but at depths of 200–300 km. The orientation of these longitudinal anomalies almost precisely parallels the direction of local gravity lineations and present-day plate motion. Forward calculations of gravity based on a velocity-temperature-density scaling were able to approximate the observed 1-D gravity variations (Eilon, Zhang, et al., 2022). This study is arguably the best observational evidence for sublithospheric oceanic SSC to date.

Surface wave analysis of data from the same array reveals low asthenospheric shear velocity of ~4.2 km/s (Russell, 2021), though not much slower than basin-wide averages at this age (Nishimura & Forsyth, 1989). More remarkably, surface waves show extremely high attenuation beneath this array with Q_S of 25–30, confined to a relatively narrow layer between 80 and 160 km depth (Russell et al., 2023). Within this same depth range, independently obtained surface wave anisotropy measurements indicate a minimum in anisotropic strength of 1.2%–2% and a transition from shallower fossil-spreading-aligned fast directions to absolute plate-motion-parallel directions (Phillips et al., 2023).

These seismological data place tacit constraints on the thermodynamic and rheological conditions in the mantle beneath the Young ORCA site, and have the potential to shed light on underlying processes. Shear velocity and attenuation have strong but distinct sensitivities to temperature, melt fraction, and grain size, among other factors (e.g., Abers et al., 2014; Faul & Jackson, 2015; Takei, 2017; Havlin et al., 2021). The seismological observations described above suggest a dynamic sub-plate system with high temperature contrasts, possibly small grain sizes, concentration of shear, and potentially heterogeneous volatiles and/or melt. Yet, to date, no study has attempted to draw together seismological and dynamical constraints to obtain a self-consistent picture of SSC that matches diverse geophysical observations.

1.2. Dynamic Models of Sublithospheric SSC

Geodynamic models allow us to quantitatively connect mantle rheology, dynamics, and seismically observable structure. Previous studies of SSC dynamics have provided numerous insights into its general mechanisms, including the expected morphology of convection rolls (Richter, 1973), their stability through time (J. Korenaga & Jordan, 2003a, 2004), their onset time and how it depends on mantle viscosity (Choblet & Sotin, 2000; Davaille & Jaupart, 1993, 1994; Dumoulin et al., 2005; Huang et al., 2003; J. Korenaga & Jordan, 2003b) and the topography of the lithosphere–asthenosphere boundary (Dumoulin et al., 2005; Huang et al., 2003), the corresponding changes in heat flux at the surface (Davaille & Jaupart, 1994; Huang et al., 2003), and its effect on melt generation and seafloor volcanism (Ballmer et al., 2007, 2009, 2010). More specific modeling studies have investigated the wavelength of longitudinal convection rolls in comparison to observed gravity lineations near the East Pacific Rise (Marquart, 2001; Marquart et al., 1999). These studies identify asthenospheric viscosity and its

gradient with depth near the base of the lithosphere—mostly controlled by the temperature-dependence—as key parameters controlling SSC onset and morphology. However, many of the complexities of asthenospheric rheology that are key to comparing geodynamic models to seismic observables have not previously been taken into account.

Asthenospheric viscosity depends on temperature, pressure, stress, and mineral grain size (among other factors). While observations of seismic anisotropy indicate that dislocation creep must play an important role in upper-mantle deformation, models investigating SSC have generally used a Newtonian rheology (Ballmer et al., 2009; Buck & Parmentier, 1986; Dumoulin et al., 2005; Huang et al., 2003; Parsons & McKenzie, 1978), with the study of Likerman et al. (2021) being a notable exception. In addition, many studies use a lower activation energy than suggested by experimental data (e.g., Hirth & Kohlstedt, 2003). Furthermore, sublithospheric SSC is an inherently three-dimensional problem and therefore requires 3D models to capture its full complexity. 2-D models can provide insight into either transverse or longitudinal modes of SSC (Huang et al., 2003), but cannot simultaneously account for up/downstream transport of material relative to the plate motion, interaction of downwellings at different plate ages, and the complex effects of shear between plate and asthenosphere (Richter, 1973; Sparks & Parmentier, 1993; van Hunen et al., 2003). Studies neglecting the interaction between these two modes cannot predict 3D convection roll morphology, and may miss fundamental aspects of SSC dynamics. Finally, existing models of sublithospheric SSC have never previously taken into account evolving mineral grain size. How SSC develops and evolves in a 3-D mantle with a composite diffusion/dislocation and grain-size-dependent rheology therefore remains an open question.

1.3. Dynamics of Evolving Grain Size

Grain size evolution may be key to the dynamics of lithospheric instabilities (Behn et al., 2009; Hall & Parmentier, 2003). Grain growth increases the diffusion viscosity, and might therefore delay the onset of SSC. By contrast, in high stress, high strain rate, or cold regions, grain size reduction caused by dislocation creep will reduce the diffusion viscosity, possibly enhancing downwelling instabilities. Grain size is therefore determined by the interplay between the two creep mechanisms (Austin & Evans, 2007), but also ensures a balance between them. Indeed, within a nascent instability, there may be a positive feedback between increased stress, high dislocation creep rate, and rapid grain size reduction that in turn leads to diffusion viscosity reduction and acceleration of material removal and increased long-term surface heat flux (Hall & Parmentier, 2003). This effect would be further enhanced by slow grain growth in (colder) downwellings that somewhat counteracts the effect of the temperature-dependence of viscosity, enabling more of the basal "lithosphere" to participate in SSC.
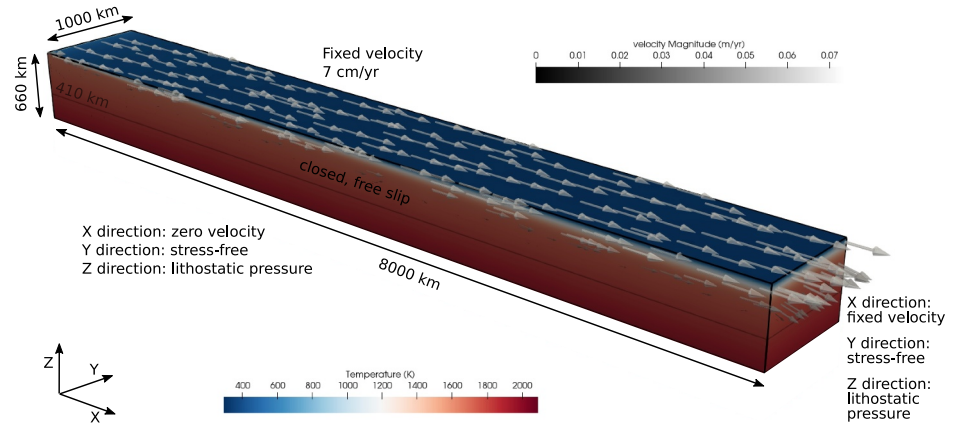
Moreover, stresses generated by the plate moving over underlying mantle enhance both dislocation creep and grain size reduction. This should spur development of convective instabilities (Hall & Parmentier, 2003). Therefore, faster plate motion (causing higher stresses) should facilitate earlier onset of SSC. This effect is not present in models using a simple Newtonian rheology.

1.4. Motivating Questions

The motivating questions for this work are: (a) Can dynamical models that include dislocation and diffusion creep and grain size evolution reproduce sublithospheric SSC, and if so, what rheological parameters are required? (b) Can those models replicate key aspects of seismological observations, and if so, how does that narrow down the rheological parameter space? (c) What type of SSC dynamics are indicated by these models, and how do these shed light more broadly on oceanic lithosphere–asthenosphere maturation?

2. Geodynamic Model Setup

To compute the geodynamic models in this study, we use the community software ASPECT (Advanced Solver for Planetary Evolution, Convection, and Tectonics; Bangerth et al., 2023; Heister et al., 2017; Kronbichler et al., 2012). We solve the equations for compressible mantle convection, considering only viscous stresses and an isotropic viscosity. We neglect terms that include the bulk viscosity and inertial terms (Schubert et al., 2001), and we use the anelastic conservation of mass equation (Jarvis & Mckenzie, 1980). In addition to the conservation of mass, we solve equations for the conservation of momentum and energy, and an evolution equation for the grain size. Our models include adiabatic heating and shear heating, resulting in the following set of equations for velocity $\mathbf{u}$, pressure P, temperature T and grain size d.

Figure 1. Setup of the geodynamic model. Colors indicate temperature, arrows indicate velocity. Model size and boundary conditions are marked by labels. Note that material is not constrained to the model domain, but rather cycles through the bottom and right model boundaries.

$$-\nabla \cdot \left(2\eta\dot{\varepsilon}\right) + \nabla P = \rho\mathbf{g}, \tag{1}$$

$$\nabla \cdot (\rho\mathbf{u}) = 0, \tag{2}$$

$$\rho C_p \left(\frac{\partial T}{\partial t} + \mathbf{u} \cdot \nabla T\right) - \nabla \cdot k\nabla T = 2\eta\dot{\varepsilon} : \dot{\varepsilon} + \alpha T(\mathbf{u} \cdot \nabla P) \tag{3}$$

$$\left(\frac{\partial d}{\partial t} + \mathbf{u} \cdot \nabla d\right) = p_g^{-1} d^{1-p_g} k_g \exp\left(-\frac{E_g + PV_g}{RT}\right) - 4\,\dot{\varepsilon}_{\mathrm{II}}\,\dot{\varepsilon}_{\mathrm{dis,II}}\,\eta_{\mathrm{eff}} \frac{\lambda d^2}{c\gamma}, \tag{4}$$

Here, η is the (effective) viscosity, $\dot{\varepsilon}$ is the deviatoric strain rate, ρ is the density, $\mathbf{g}$ is the gravity vector, C_p is the specific heat capacity of the material, k is the thermal conductivity, and α is the thermal expansion coefficient. Equation 4 describes the grain size evolution as the sum of a grain growth term, approximated using a semi-empirical expression (e.g., Austin & Evans, 2007; Burke, 1949), and a grain size reduction term, approximated by the paleo wattmeter (Austin & Evans, 2007), which assumes that a certain fraction of the work done by dislocation creep goes into reducing the grain size. p_g is the grain growth exponent, k_g is an experimentally determined prefactor, E_g and V_g are the grain growth activation energy and volume, R is the gas constant, c is a geometric constant, λ is the fraction of work that goes into changing the grain boundary area, and γ is the average specific grain boundary energy. $\dot{\varepsilon}_{\mathrm{II}}$ indicates the square root of the second invariant of the strain rate tensor, and $\dot{\varepsilon}_{\mathrm{dis}}$ is the part of the strain rate accommodated by dislocation creep. More details on this formulation can be found in Dannberg et al. (2017), and all material properties are given in Table S1 in Supporting Information S1.

Our model domain has a 3D Cartesian geometry featuring a plate moving away from a mid-ocean ridge. The model is 8,000 km long in the direction of spreading, 1,000 km wide in the transverse direction, and extends 660 km or 1,000 km in vertical direction (see Figure 1). We use an adaptive mesh with a maximum resolution of $5.2 \times 3.9 \times 5.2$ km and track the evolution of the mineral grain size on particles (for details see Text S1 in Supporting Information S1).

2.1. Initial and Boundary Conditions

The initial temperature follows a half-space cooling model with a surface temperature of 293 K added to an adiabatic profile with a potential temperature of 1,623 K, using a constant thermal diffusivity of 6.0833×10^{-7} m^2/s. The initial plate age used to compute the half-space cooling temperature assumes a constant plate speed of 7 cm/yr away from the ridge. In addition, we add 5,000 small Gaussian temperature perturbations at random locations and with a random amplitude of up to ± 5 K and a sigma of 60 km. To prevent numerical instabilities due to the change in velocity at the ridge axis, we add a 2D Gaussian temperature anomaly with an amplitude of 500 K

and a width of 10 km at the edge of the model located at the ridge, reducing the viscosity. The initial grain size is set to 5 mm, except for a 2D Gaussian anomaly with a sigma of 30 km centered 13 km below the ridge axis, where the grain size is gradually reduced to a minimum of 2 mm, facilitating deformation at the ridge.

We prescribe the plate velocity of 7 cm/yr at the top boundary of the model. To ensure a reasonable vertical velocity gradient within the mantle, we set the component of the velocity pointing in the direction of spreading to zero at the base of the model. In the other directions, the bottom boundary is free of deviatoric stress, providing no resistance to vertical inflow and outflow of material. The model boundary at the mid-ocean ridge ($x = 0$ km) is closed, but allows for free slip in the vertical direction. At the boundary furthest from the mid-ocean ridge ($x = 8000$ km), we fix the velocity to be parallel to spreading, causing material to flow out of the model domain. To minimize the effect of the boundary conditions, we base this velocity profile on the flow that would develop under lithostatic pressure conditions without SSC: Above 140 km depth, the prescribed outflow velocity equals the plate velocity, then it linearly decreases to 0.5 cm/yr at 270 km depth, and then again from 0.5 cm/yr to 0 at 410 km depth. Below that depth there is no in- or outflow. The transverse (ridge-parallel) velocity component at the boundary $x = 8000$ km is set to zero, and the vertical direction is stress-free. The sides of the model parallel to the spreading direction are closed, but stress-free in all tangential directions. The temperature is fixed to 293 K at the surface. Additionally, at the parts of the boundary where there is inflow of material into the model, both temperature and grain size are fixed to the same value as in their initial conditions. We let all models evolve for 100 Myr.

2.2. Rheology

Our models use a combined diffusion and dislocation creep rheology. Important distinctions are that the diffusion creep viscosity η_{diff} depends on grain size, while the dislocation creep viscosity η_{dis} depends on the stress/strain rate. We use the same rheological models as in Dannberg et al. (2017), leading to the following expressions:

$$\eta_{\text{diff}} = \frac{1}{2} A_{\text{diff}}^{-1} \, d^m \, \exp\left(\frac{E_{\text{diff}} + P V_{\text{diff}}}{RT}\right), \tag{5}$$

$$\eta_{\text{dis}} = \frac{1}{2} A_{\text{dis}}^{-\frac{1}{n}} \, \dot{\varepsilon}_{\text{dis,II}}^{\frac{1-n}{n}} \, \exp\left(\frac{E_{\text{dis}} + P V_{\text{dis}}}{nRT}\right), \tag{6}$$

and the effective viscosity

$$\eta_{\text{eff}} = \frac{\eta_{\text{diff}} \, \eta_{\text{dis}}}{\eta_{\text{diff}} + \eta_{\text{dis}}}. \tag{7}$$

Where A is a constant prefactor, m is the grain size exponent, n is the stress exponent and all other parameters as defined above. The rheological parameters depend on the stable mineral phases, therefore we consider different values in the upper mantle compared to the transition zone (see Tables S1 and S2 in Supporting Information S1). For computational efficiency, we limit the maximum effective viscosity η_{eff} to 10^{23} Pa s, a value that prevents almost all deformation in the cold lithosphere.
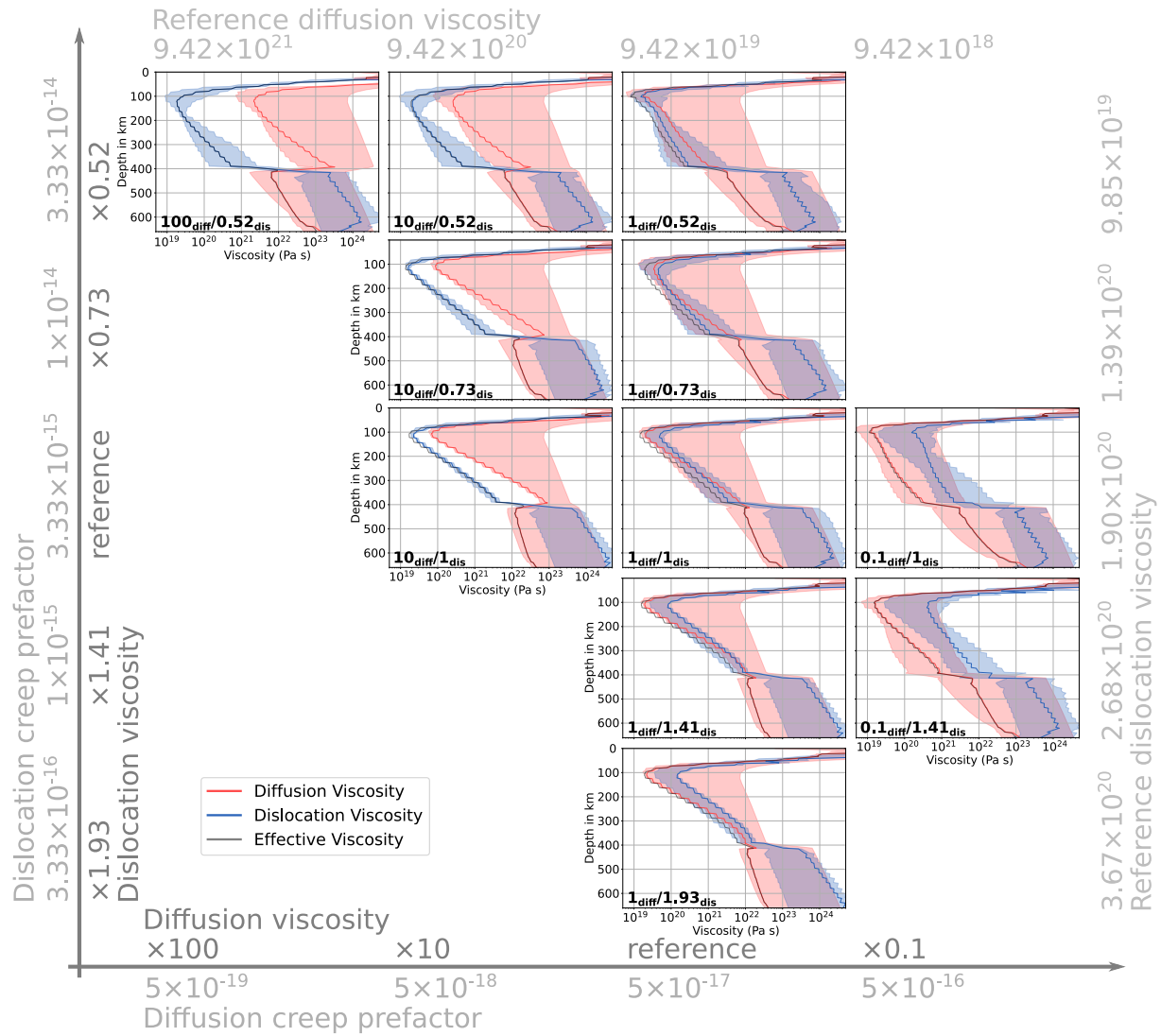
Since the observables we are interested in—the location, amplitude and morphology of the cold downwellings from the base of the lithosphere—depend on the viscosity, we ran several simulations, varying the diffusion and dislocation creep prefactors in the upper mantle compared to the experimentally derived values, with all parameter combinations given in Table S2 in Supporting Information S1. The resulting viscosity profiles at 42 Ma plate age are shown in Figure 2. The prefactors affect both the effective viscosity and the balance between diffusion and dislocation creep. The diffusion viscosity is highly variable over time due to the evolving mineral grain size.

2.3. Other Material Properties

We use a simplified equation of state in the form

$$\rho(P, T) = \rho_0 \exp(\kappa_T \, P)(1 - \alpha(T - T_{\text{ref}})) \tag{8}$$
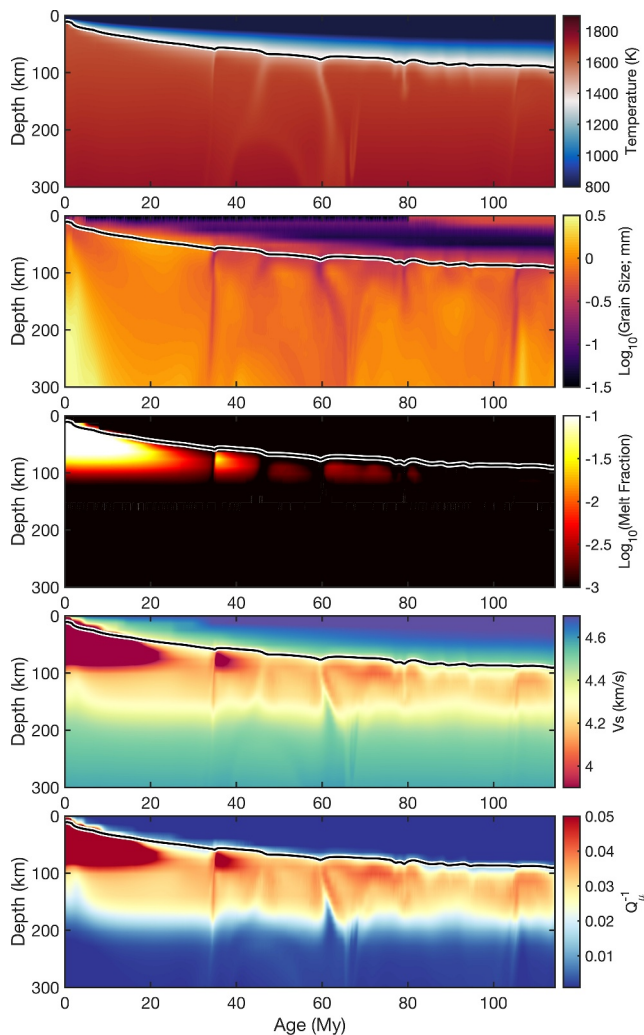
Figure 2. Viscosity profiles for different models at a distance of 2,940 km from the ridge (42 Ma plate age), averaged (using the log-average) across all values in ridge-parallel (*y*) direction. Solid lines show the temporal average over the whole model time, shaded areas show variations between the minimum and maximum viscosities at different points in time. See Table S2 in Supporting Information S1 for details on how reference viscosities are defined.

with a constant isothermal compressibility κ_T and thermal expansivity α, and the reference temperature $T_{ref} = 293$ K. All parameter values are given in Table S1 in Supporting Information S1.

The thermal conductivity is temperature- and pressure dependent following the equation

$$k(P,T) = k_{298}\left(\frac{298.0}{T}\right)^{a} \exp(-(4\gamma + 1/3)\alpha(T - 298))\left(1 + K_0'\frac{P}{K_0}\right)$$
$$+ 0.01753 - 0.00010365T + 2.2451 \times 10^{-7}T^2 - 3.407 \times 10^{-11}T^3 \tag{9}$$

with $k_{298} = 4$ W/(m K) the lattice thermal conductivity at the ocean floor, $a = 1/3$ (for silicates), $\gamma = 1.2$ the Gruneisen parameter, $K_0 = 135$ GPa the bulk modulus, and $K_0' = 4$ the pressure derivative of the bulk modulus. While the equation is from Hofmeister (1999), we here use the parameter values from Honda and Yuen (2001, Equation 1), a study that fits the Hofmeister (1999) model to ocean floor depth and heat flux of GDH1 (a theoretical thermal model of the oceanic lithosphere). The temperature-dependence causes a decrease in thermal

Figure 3. Vertical cross-sections through model 7 ($1_{diff}/0.52_{disl}$) at model time of 80 My and associated seismic properties calculated at 65 s period assuming 100 ppm H_2O + 100 ppm CO_2. Physical properties temperature and grain size are output from ASPECT. Melt fraction is calculated in post-processing using a hydrous equilibrium melting model (Blatter et al., 2022). Shear velocity (V_S) and attenuation (Q_{μ}^{-1}) are calculated using the VBRc (Havlin et al., 2021) and Perple_X (Connolly, 2005; Connolly & Kerrick, 1987). The black contour in each panel marks the 1150°C isotherm, temperatures below which are assumed to represent dehydrated mantle.

conductivity with increasing temperature, leading to a hotter base of the plate and a steeper thermal gradient compared to a model with a constant thermal conductivity (Honda & Yuen, 2001).

Methods for computing the heat flux and dynamic topography are described in Text S2 in Supporting Information S1. Additional model postprocessing steps and model limitations are discussed in Texts S3 and S4 in Supporting Information S1, respectively.

3. Synthetic Seismology

3.1. Calculating Seismic Properties From Model Outputs

"Translating" geodynamical model outputs to seismic properties requires a multi-stage process. First, we use temperature and pressure to calculate a stable mineralogy and unrelaxed bulk and shear moduli and density for the aggregate using Perple_X (Connolly, 2005; Connolly & Kerrick, 1987), assuming a pyrolite bulk composition. We consider five possible scenarios of CO_2 and H_2O bulk concentrations: volatile-free; 0 ppm CO_2 + 100 ppm H_2O; 0 ppm CO_2 + 250 ppm H_2O; 100 ppm CO_2 + 100 ppm H_2O; and 100 ppm CO_2 + 250 ppm H_2O. These scenarios are chosen to span the range of prior estimates for the upper mantle (Dasgupta et al., 2007, 2013; Hirschmann, 2006; Hirth & Kohlstedt, 1996; Michael, 1988). To mimic a dehydrated lithosphere (Hirth & Kohlstedt, 1996), we set the volatile content to 0 ppm wherever temperatures <1150°C. For each volatile scenario, we calculate solidi and batch melt fractions using the approach of Blatter et al. (2022), assuming the system is in equilibrium and melt remains in situ. To be clear, we impose these volatiles and partial melt as a post-processing step; no volatile or melting effects on either viscosity or density are incorporated in the dynamical models. We are aware that this may lead to some inconsistency in effective viscosity between the modeled viscosities and those implied by our post-processing calculations. The magnitude of this discrepancy is a factor of ∼3 on average, as captured in Figure S1 in Supporting Information S1.

Using the temperature, pressure, diffusion creep viscosity, and grain size from the ASPECT models, together with unrelaxed elastic moduli and density from Perple_X, and computed solidii and melt fractions, we calculate viscous and anelastic parameters using the Very Broadband Rheology calculator (Havlin et al., 2021, see Figure 3). We assume mantle anelasticity in line with the "premelt" model (Yamauchi & Takei, 2016) and account for melt affecting anharmonic moduli through the poroelastic effect (Takei, 2002) as well as directly affecting anelasticity and viscosity through grain boundary effects (Yamauchi & Takei, 2024). Volatiles impact viscosity indirectly through solidus depression and activation of the premelt effect (Yabe et al., 2020; Yabe & Hiraga, 2020). We do not explicitly include a direct effect of water on viscosity (Hirth & Kohlstedt, 1996) because our variation of the flow law prefactors in the ASPECT simulations (Section 2.2) is akin to this effect, with larger prefactors corresponding to a wetter (and weaker) mantle. These calculations provide "translated" anelastic seismic properties at all model nodes at periods of 65, 10, and 1 s representing the dominant frequencies of the surface-wave, S-, and P-wave observations, respectively.

3.2. Computing Synthetic Seismic Data

We compare the "translated" ASPECT model to surface wave observations in both model space (average profiles of V_S and Q_{μ}^{-1}) and data space (average Rayleigh phase velocity and attenuation). The latter provides more direct comparison to true data, since the 1-D V_S and Q_{μ}^{-1} "observed" models are obtained via regularized inversion.

First, we extract V_S and Q_μ^{-1} from the "translated" ASPECT model within a $\sim 500 \times 500$ km^2 footprint centered at $x = 2{,}940$ km (~ 42 My) to mimic the Young ORCA array site. We replace the upper ~ 6.4 km of the ASPECT model domain with realistic oceanic crust from Russell et al. (2019) and drape a 4,625 m thick water layer on top. We forward calculate Rayleigh wave phase velocity and attenuation dispersion from the translated model for each vertical profile within the $\sim 500 \times 500$ km^2 footprint using the SURF96 layered model dispersion code (Herrmann, 2013). Since Rayleigh waves are primarily sensitive to vertically polarized shear waves V_{SV}, we convert the ASPECT model to V_{SV} using radial anisotropy $\left(\xi = V_{SH}^2/V_{SV}^2\right)$ from the regional model of Nishimura and Forsyth (1989) and the relationship $V_{SV} = V_S\sqrt{3/(2 + \xi)}$.

For synthetic body wave tomography, we construct an array of synthetic OBS instruments with the same configuration as the ORCA arrays (Eilon, Gaherty, et al., 2022), including orientation with respect to plate motion. For comparison to the data, the array is centered at the Young ORCA age ($x = 42$ Ma $\times$ 7cm/yr $= 2940$ km), and we set the ridge-parallel (y) location to ensure the array spans multiple convective downwellings, as the Young ORCA array appears to. We construct a synthetic seismic catalog of 50 shallow mantle events randomly distributed between 30 and 85° in distance from the center of our array. The events have semi-random back-azimuthal distribution, whereby we prescribe four random 40° gaps in the angular distribution of sources. This catalog mimics the characteristics of mid-Pacific temporary OBS deployments. We trace rays in 1-D from all stations toward all sources within a 800×800 km model space centered on the array, using an average velocity profile from the youngest edge of the model space (i.e., avoiding any SSC cells). We calculate finite frequency travel-time sensitivity kernels using the first fresnel zone paraxial approximation to the full Born kernel (Brunsvik et al., 2021; Schmandt & Humphreys, 2010) and assuming center frequencies of 1 and 0.1 Hz for *P*- and *S*-waves respectively (we focus on *P*-waves for comparison to the existing observations, providing *S*-wave synthetics in Supporting Information S1). Synthetic differential travel times are computed by multiplying these kernels with the input velocity structures derived from the "translated" ASPECT models linearly interpolated onto a dense local grid. Finally, we invert these travel times (which are de-meaned by event, to mimic the process of cross-correlation) using regularized least squares, where both norm damping and first-derivative flattening are imposed. We go through this process of inverting synthetic data to understand not only the 3-D features predicted to appear in seismological models, but also which features may be distorted or obscured by the process of tomography: the "tomographic filter."
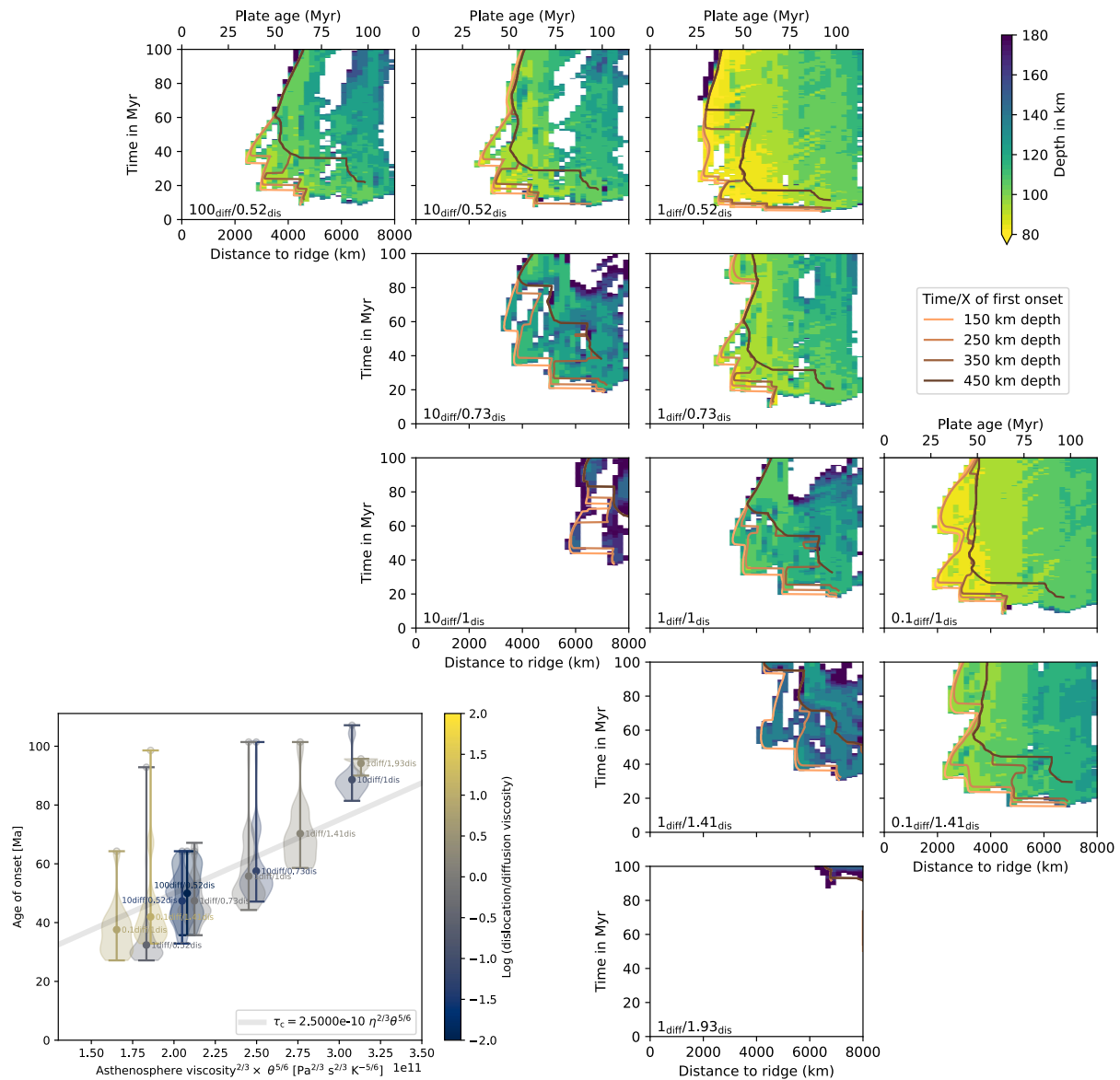
4. Geodynamic Modeling Results

4.1. Convection Regimes and Morphology of Cold Downwellings

In all models, there is an interplay of diffusion creep, dislocation creep, and grain size evolution. However, the balance between diffusion and dislocation creep depends on the flow law parameters (see Figure 2; the balance changes from top left to bottom right). In models with a higher diffusion viscosity prefactor (thus lower diffusion viscosity), diffusion creep dominates. Conversely, dislocation creep dominates in models with a high dislocation creep prefactor. The exact balance of deformation mechanisms depends on the temperature/pressure/strain rate/grain size conditions (see also Figure 4 and Movies S3–S6), and in turn also controls grain size evolution. For example, models with more dislocation creep generally have lower grain sizes (see Figure S2 in Supporting Information S1).

Initially, all models have a similar flow field due to the boundary conditions. Away from the in-/out-flow boundaries, most material flows horizontally, with horizontal shear due to plate motion. At the outset, most of this shear deformation is concentrated over a narrow range near the top of the asthenosphere where the viscosity is lowest (see Figure 2). Over time, the cold top boundary layer becomes unstable and triggers the onset of SSC. The specific time of onset depends on the model parameters (see Section 4.2).
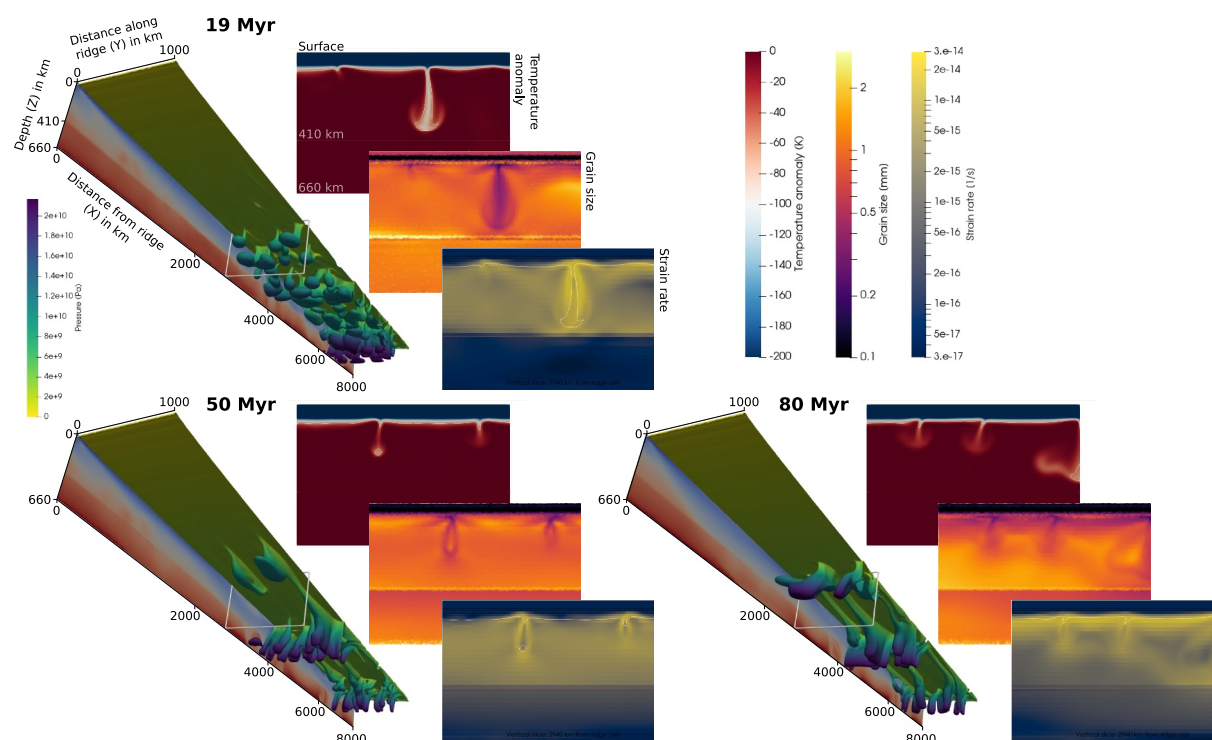
In all models, SSC first manifests as longitudinal convection rolls. This agrees with theoretical predictions (Richter, 1973) and observations (Eilon, Zhang, et al., 2022). Due to the random initial temperature perturbations, these structures feature spatial temperature variations, both along their axes and between rolls (see Movies S3–S6). The lower the asthenospheric viscosity, the stronger these variations, with some models featuring initial cold "plumes" coalescing into downwelling sheets/convection rolls and others forming downwelling sheets from the outset.

Figure 4. Shallowest depth where SSC occurs (defined as the 0.1%-th percentile of the vertical velocity among all the points in a depth range of ±25 km exceeding 1 cm/yr in downwards direction) in dependence of distance from the ridge (plate age) and point in time during model evolution. White colors indicate no SSC. Orange/brown solid lines highlight youngest plate age (expressed as distance from the ridge) where >1 cm/yr downwelling occurs at a given time for four different depths. Bottom left inset shows the relation between effective viscosity and Frank-Kamenetskii parameter computed from the flow law parameters versus the onset time of SSC. The violin plots show minimum, maximum, mean (solid circle), and initial (empty circle) onset time, with the violin color representing the diffusion/dislocation creep ratio at the mean effective viscosity and the violin width representing the fraction of the model evolution time that features a given SSC onset age. The gray line represents the least squares fit of a line $y = ax$ through the mean onset times. How the age of onset depends on the individual diffusion and dislocation creep viscosities is shown in Figure S13 in Supporting Information S1.

In a ridge-parallel cross-section, the downwelling sheets have a plume-like shape with broad tips from the initial instability and thinner conduits connecting them to the lithosphere (Figure 5). Since viscosity gradually increases with depth, followed by an abrupt increase at 410 km depth (see Figure 2), the downwellings slow between ∼200 and 350 km depth, causing broader cold anomalies in that depth range (see also Section 4.4). Eventually, this cold material breaks through the 410-km-depth transition, sinking further downward and leaving the model through the bottom boundary. The width and temperature anomaly of the downwellings depend on the viscosity as controlled by the flow law parameters—with lower viscosity leading to thinner downwellings (compare Movies S3 and S6).

Figure 5. Evolution of the best-fit model $1_{\text{diff}}/0.52_{\text{dis}}$ at three different times. Left panels show a view from below with temperature contours 20 K below the adiabat colored by pressure. Panels on the right show the temperature, grain size and strain rate distribution in vertical slices at 42 Ma plate age/2,940 km from the ridge. For the full model evolution, see Movie S3.

The onset of SSC alters the temperature, strain rate, and grain size of the asthenosphere. Due to the removal of cold material, temperatures near the base of the plate are higher (in comparison to a plate of the same age, but without SSC). This could allow for mantle melting, especially if any upwelling material is fertile and/or volatile-rich (see also Section 5.1). In addition, following SSC onset, the strain rate increases throughout the upper mantle and its maximum shifts to shallower depth, as strain localizes at the base of the lithosphere where the cold drips form (Movies S3–S6). This faster deformation is not only present at the locations of the cold downwellings, but extends horizontally along the base of the lithosphere (Figure 5). The localized deformation reduces the grain size and increases its lateral variations. After SSC onset, the minimum in grain size is therefore smaller and shifted shallower. Within the cold downwellings, grain size is reduced drastically (to a median of well below 1 mm and a minimum below 200 μm, with the exact values depending on the flow law parameters, see Figure S2 in Supporting Information S1). This owes to the combination of large strain rates and slow grain growth. On the other hand, the grain size deeper in the asthenosphere, between the cold drips, tends to become even larger than before SSC, since the plate-motion-driven shear deformation (and associated grain size reduction) is focused in a thin layer at the base of the plate (Figure 5). An interesting corollary to these grain size dynamics is that the cold downwellings' interiors are not appreciably more viscous than the surrounding mantle. Even though they may be up to 100 K colder than the mantle adiabat, the small grain sizes in their interiors offset the effect on viscosity. The drips are surrounded by an envelope of low-viscosity warmer asthenosphere, since deformation localizes at their edges.

The onset of sublithospheric convection marks only the first shift in model evolution. Although longitudinal convection rolls are the expected planform of convection at its onset, it has been shown that they can become unstable to three-dimensional perturbations—in particular at high Rayleigh numbers—so that the planform of fully evolved convection may deviate from longitudinal rolls and become multimodal (J. Korenaga & Jordan, 2003a). We do find that the character of convection changes when the cold downwellings break through the transition zone, marking the shift from (layered) upper mantle convection to whole-mantle scale sublithospheric convection (as discussed in J. Korenaga & Jordan, 2004, for the 2D case).

In our models, this breakdown manifests itself by the establishment of long-wavelength transverse convection cells. These have downwellings concentrating at ∼4,300 and 6,800 km from the ridge axis (or 61 and 97 Ma plate age; see Figure S3 in Supporting Information S1 and Movies S3–S5) and upwellings in between. The ∼2,500 km wavelength of these larger, transverse convection cells is not per se dependent on the asthenospheric flow law parameters, since it is controlled by the (fixed) viscosity of the layer below (in addition to the time taken for the lithosphere base to reach critical thickness). This is demonstrated by our models with different transition zone diffusion creep prefactors (see Figure S3 in Supporting Information S1 bottom row, Table S2 in Supporting Information S1). However, the larger-scale downwellings need to develop from an upper mantle that has already initiated small scale convection. Thus, the 4,300-km-distance drip only forms in models with young (<60 Ma) SSC. In more viscous models (e.g., $1_{\text{diff}}/1.93_{\text{dis}}$) where almost the whole 100 Myr model evolution time is required before downwellings interact with the model base, the transverse convection cell does not have a chance to even develop within our models.

4.2. Onset Time of SSC

Two main controls on the onset time of SSC identified by previous studies (Davaille & Jaupart, 1993, 1994; Dumoulin et al., 2005; Huang et al., 2003; J. Korenaga & Jordan, 2003b) are the interior Rayleigh number Ra_i (taken at the average interior temperature of the model T_i, excluding boundary layers) and the temperature-dependence of viscosity, which can be described using the Frank-Kamenetskii parameter

$$\theta = -\left.\frac{d \ln \eta(T)}{dT}\right|_{T=T_i} = \frac{E+PV}{RT_i^2} \tag{10}$$

for an Arrhenius flow law as used in our models. The onset time τ_c is often expressed in a scaling law of the form
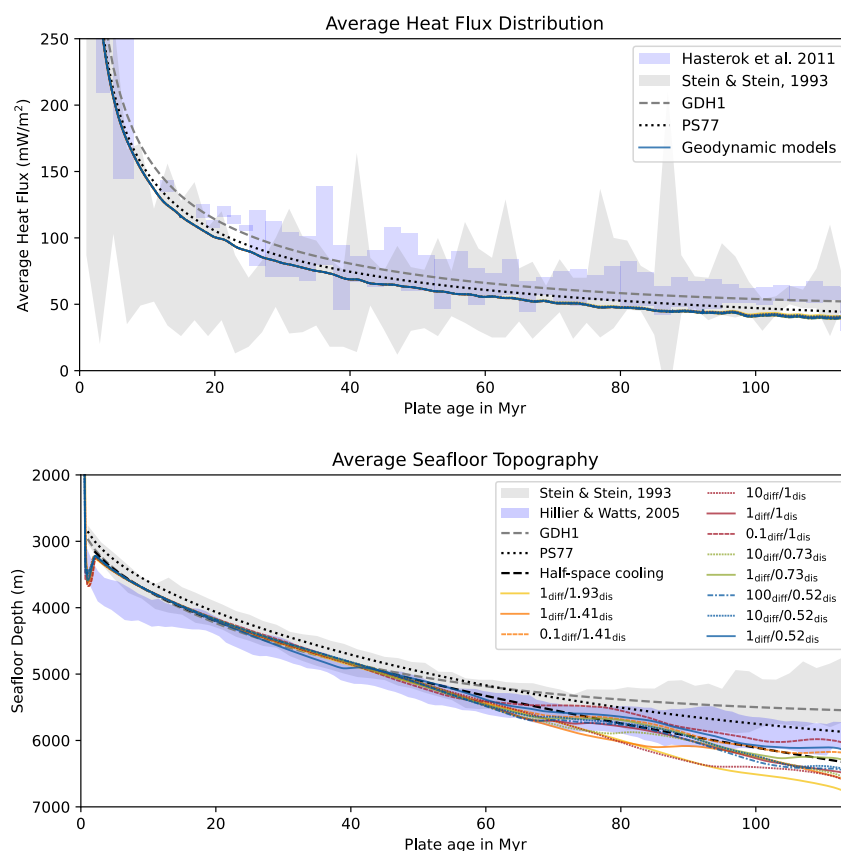
$$\tau_c \propto Ra_i{}^a \theta^b \tag{11}$$

with a and b being constants. In the following, we will use this relation to analyze the onset time of convection in our models (for details, see Text S5 in Supporting Information S1). While these scaling laws account for temperature-dependence of viscosity (and, in the case of J. Korenaga & Jordan, 2002, a viscosity jump with depth), they neither incorporate the effect of dislocation creep/strain-rate dependence nor an evolving grain size. With all these complexities included (and a depth- and temperature dependent thermal conductivity), it becomes difficult to define Ra_i consistently. It is beyond the scope of this study to develop a scaling law that would include these additional complexities. However, plotting our results against existing scaling relationships highlights the general effect of a non-linear rheology.

The inset in Figure 4 displays the positive scaling between the onset time of SSC and $\eta_{\text{eff}}{}^{2/3}\theta^{5/6}$. We highlight both the mean onset time and its spread throughout the model evolution time. The onset time can be fit reasonably well with the existing scaling law even for a nonlinear rheology, showing the balance between diffusion and dislocation creep (indicated by color) does not systematically affect the slope of the linear relationship.

Only the models with a large viscosity show substantially later onset times than predicted by the scaling law. This may be explained by two different factors. First, we may be underestimating true viscosity in this analysis because we use the same T_i and P in all flow laws. In reality, the top of the asthenosphere is at higher pressures (and therefore slightly higher viscosities) under older parts of the plate. Second, sublithospheric SSC only occurs very late during the model time and/or near the model boundary in these models (see panels $1_{\text{diff}}/1.93_{\text{dis}}$ and $10_{\text{diff}}/1_{\text{dis}}$ in Figure 4), and thus may not represent a stationary sample of model behavior or may be affected by the boundary conditions.

All models with SSC over a longer (>70 Myr) extent of model time show a distinct evolution in its onset time. After the first downwelling occurs at a given distance from the ridge axis, subsequent instabilities occur at younger plate ages, initially causing a step-wise decrease in the minimum plate age where SSC occurs. Afterward, the onset age periodically varies around some average, representing downwellings carried toward older plate ages together with the plate-driven flow in the asthenosphere and the later onset of a new downwelling at a younger plate age. While this quasi-steady behavior is expected for convective instability, the initial step-wise decrease in onset age with increased model time highlights the effect of dislocation creep and grain-size-dependent rheology.
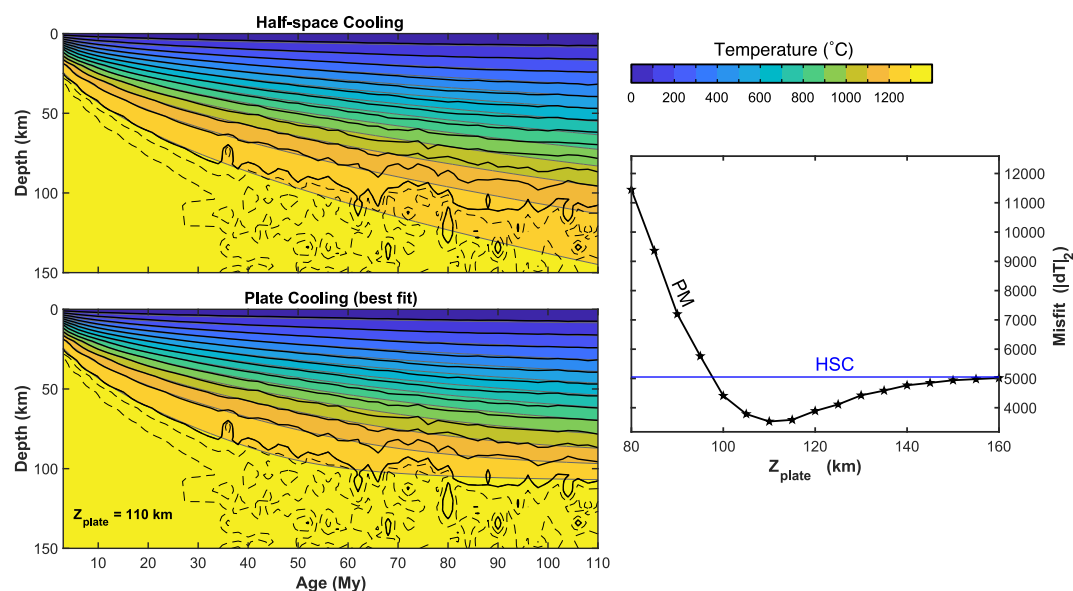
Figure 6. Heat flux and seafloor depth versus age relationship in our models. Colored lines represent the average heat flux (top) and seafloor topography (bottom) at the end time (after 100 Myr of model evolution) of the geodynamic models, with the color indicating the rheologic parameters used in each model. The heat flux includes an added correction for radiogenic heat production (0.5 mW/m^2, Hasterok, 2010). In terms of their heat flux, the different models are almost indistinguishable and plot on top of one another. The gray area illustrates the heat flux and topography data from Stein and Stein (1993) (which includes anomalous topography such as seamounts), with their fit to the data (GDH1 model) shown as a dashed line. The plate model from Parsons and Sclater (1977) is shown as dotted line. The blue shaded area represents the more recent data: Sediment-corrected heat flux data from Hasterok et al. (2011) (top) and topography data from Hillier and Watts (2005) (which removes seamounts, oceanic islands, oceanic plateaus, and midplate topographic swells).

During the initial phase of conductive cooling, the strain rate is low and grain size is large. The descent of the first downwelling increases the strain rate (reducing dislocation viscosity) and, consequently, decreases the grain size in the surrounding asthenosphere (decreasing diffusion viscosity). Subsequent instabilities can therefore develop more readily, at younger plate ages. Because both diffusion and dislocation creep are affected, this behavior is visible in all of our models (Figure 4).

4.3. Model Validation: Heat Flux and Seafloor Topography

To ensure that our geodynamic models capture the first-order effects of oceanic plate cooling and evolution, we compare age-dependent heat flux and seafloor topography to observations. We evaluate both properties at the end of our model evolution (100 Myr). Our models do not include radiogenic heating, so we add heat flux estimated from radiogenic heat production within oceanic plates (0.5 mW/m^2, Hasterok, 2010) to our computed heat flux. Since this heat is mainly generated in the oceanic crust, we treat it as a constant value (~0.35 mW/m^2). The resulting heat flux versus age relationship (Figure 6 top) shows a reasonable agreement with previous models and heat flux measurements. Our modeled heat flux lies at the lower end of the observed heat flux data and is slightly lower (by ~5 mW/m^2) than the model of Parsons and Sclater (1977) but shows the same flattening with age. Note that for models with SSC, heat flux may not be in steady state; it takes some time for associated thermal anomalies to propagate to the surface (Davaille & Jaupart, 1994), potentially several times the onset time (Huang

Figure 7. Temperature comparison between standard lithospheric cooling models and "best-fit" ASPECT model (Section 4.5). Colors indicate 100 K contours for plate cooling (bottom left, "PM") and half-space cooling (top left, "HSC"), where the former is shown for the best-fitting plate thickness (110 km). Overlaid black contours are the 100 K isotherms from a 2-D average of the ASPECT model at 80 My model run time (with thin dashed contours at 1320°C and 1340°C). For both models, the misfit as a function of plate thickness is shown on the right. Potential temperature and temperature-dependent thermal diffusivity are the same as for the ASPECT calculations. Note, although SSC onset is ∼30 My, significant departure from the half-space-cooling plate thickness is not until ∼60 My.
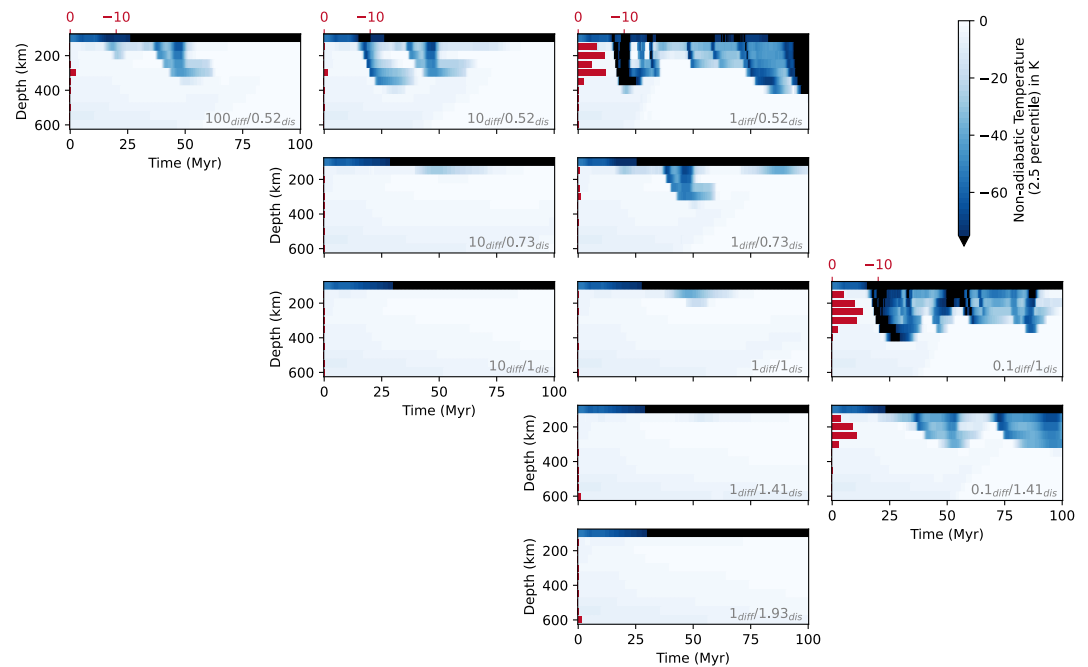
et al., 2003). This is not, per se a flaw—in the event that time-varying SSC processes take place in oceanic upper mantle, the true ocean basins' heat flux should similarly never reach steady state. All that said, we find that SSC does not substantially change the surface heat flux, consistent with prior work (J. Korenaga & Jordan, 2002). This is because only a thin layer at the base of the lithosphere becomes convectively unstable, and only small portions drip off at once. Therefore, temperature variations and the corresponding change in plate thickness are small (Figure 7) and heat flux anomalies are smoothed by the thick lid (Davaille & Jaupart, 1994).

While all our models show similar heat flux versus age, they differ more substantially in their predictions of seafloor depth versus age (Figure 6 bottom). For older seafloor (>70 Ma), several of the models clearly predict a greater seafloor depth than is observed, even with anomalous topography (such as from seamounts and ocean islands) removed from the data (Crosby et al., 2006). Generally, models that have a lower effective asthenospheric viscosity (high values for both diffusion and dislocation creep prefactor, top right panels in Figure 2) have a shallower seafloor depth for these old ages, yielding a better fit to the observations. The three models with the shallowest seafloor depth are $0.1_{diff}/1_{dis}$ (yellow line), $1_{diff}/0.52_{dis}$ (lightest pink line), and $0.1_{diff}/1.41_{dis}$ (light green line) which all yield viscosity $<2 \times 10^{19}$ Pa s in the asthenosphere. These are also the models with the earliest onset age of SSC (Figure 4).

4.4. Amplitude, Depth, and Wavelength of Thermal Anomalies at 42 Ma Plate Age

To compare our models to the seismic observations of apparent SSC from the Young ORCA array, we analyze the temperature distribution in our models at a plate age of 42 Ma (a distance of 2,940 km from the ridge axis). The negative temperature anomalies (Figure 8) illustrate that SSC occurs at such a young plate age only in models with a low asthenospheric viscosity (below ∼2 × 10^{19}, compare Figure 2), in agreement with the scaling law (see Figure 4). However, in most of the simulations, these downwellings only occur over short periods, infrequently throughout the model evolution and/or the amplitude of the temperature anomalies remains below 75 K, which makes it more difficult to explain the observed seismic anomalies. Only for the two models with the lowest viscosity ($0.1_{diff}/1_{dis}$ and $1_{diff}/0.52_{dis}$) does SSC yield downwellings with temperature anomalies consistently above 75 K (and maximum anomalies of more than 90 K) that remain active throughout the model evolution (after its onset).
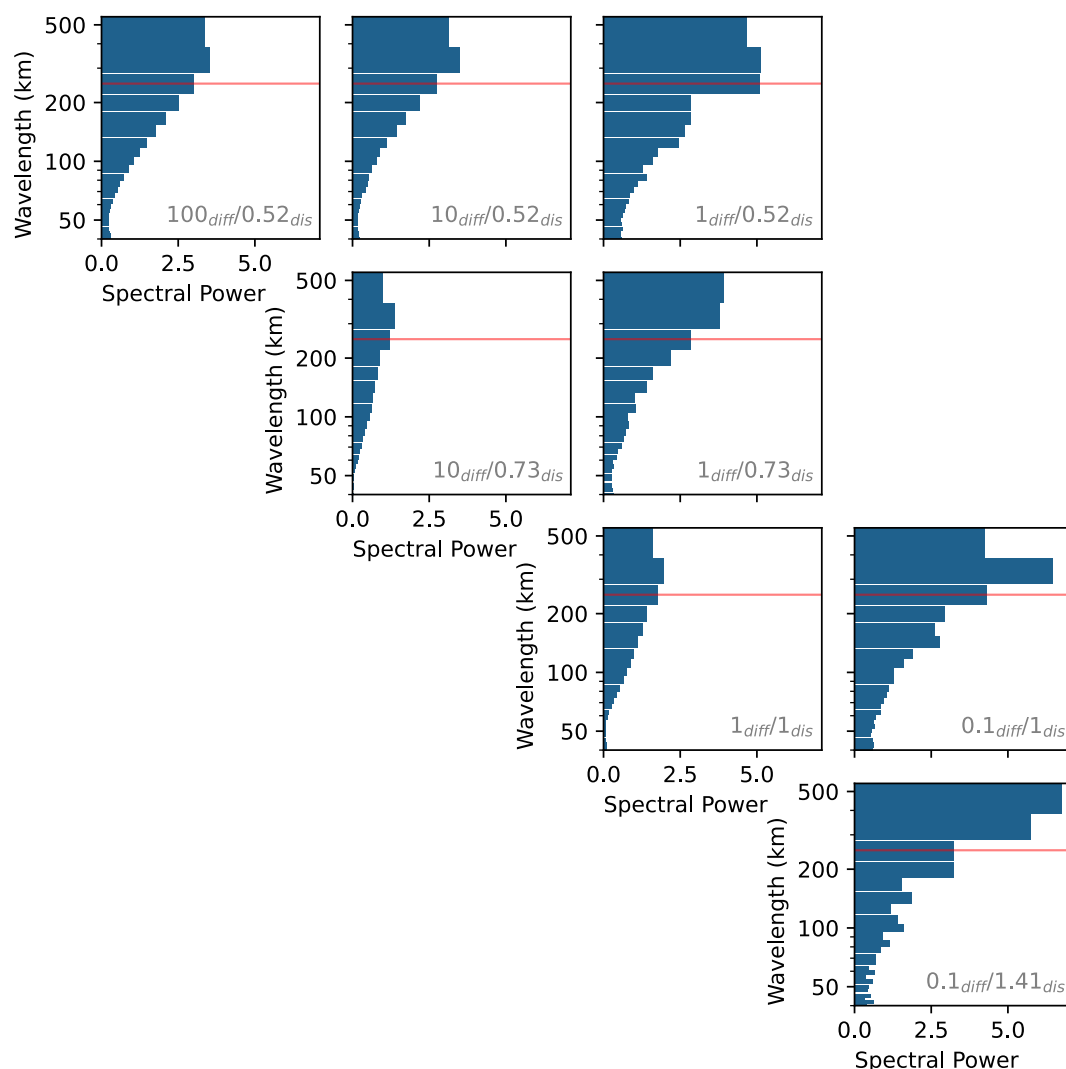
Figure 8. 2.5 percentile of the temperature anomaly (compared to the adiabatic profile with $T_p = 1623$ K) in ridge-parallel (y) direction at a plate age of 42 Ma, plotted in dependence of time and depth for all models. Blue streaks sloping downward indicate cold downwellings from the base of the plate. Temperature anomalies below -75 K are shown in black. Red horizontal bars indicate the mean temperature anomaly in K averaged over the whole model evolution time for each depth range below 100 km. Panels are arranged as in Figure 2.

Figure 8 also provides insights into the depth distribution of the temperature anomalies. While cold downwellings cause negative temperature anomalies across a broad depth range, they stop at ∼400 km depth because of the viscosity increase from the upper mantle to the transition zone at 410 km depth, which slows down convective motion. In addition, below 120 km depth the viscosity in the asthenosphere generally increases with depth in our models (see Figure 2), so that downwellings developing at the base of the lithosphere can sink quickly at first, but slow down as they sink further (visible in the flattening of the downward slopes of the blue streaks in Figure 8). Therefore, in models with SSC, the temperature anomalies do not simply diminish with depth. Instead, temperature anomalies are large within the lithosphere due to the cold plate, low in the sublithospheric mantle just below the base of the plate, and have a maximum in a depth range of 200–300 km depth (Figure 8, red bars). This pattern closely mimics the depths of strongest anomalies observed by seismic tomography (Eilon, Zhang, et al., 2022).

To analyze the wavelength of the convection rolls in our models, we computed the power spectra of the longitudinal structure of the temperature anomaly compared to the initial adiabat at 42 Ma plate age during the model times when downwelling occurs (Figure 9). While the spectral power is generally substantial for wavelengths between 100 and 500 km, our analysis reveals that the largest possible length scales of 300–500 km dominate the convection pattern in most models. Only in model $0.1_{diff}/1_{dis}$, the wavelength of 300–400 km is by far stronger than 400–500 km, and model $1_{diff}/0.52_{dis}$ features the strongest power in the 200–300 km and the 300–400 km wavelength, which have approximately equal amplitude. Therefore, only the latter two models can be considered comparable to the observations from seismology and gravity, which suggest a length scale of the convection rolls of ≈250 km.

Overall, only in the two models with the lowest viscosity ($0.1_{diff}/1_{dis}$ and $1_{diff}/0.52_{dis}$) do we find SSC with temperature anomalies that exceed 75 K, remain active throughout the model evolution after its onset, and match the tomographically observed wavelength and depth range. However, model $0.1_{diff}/1_{dis}$ is dominated by diffusion rather than dislocation creep in the asthenosphere, which is inconsistent with observations of seismic anisotropy. Additionally, the wavelength of the convection rolls is somewhat larger than observed. Therefore, $1_{diff}/0.52_{dis}$ is the model that best matches the constraints from seismology.
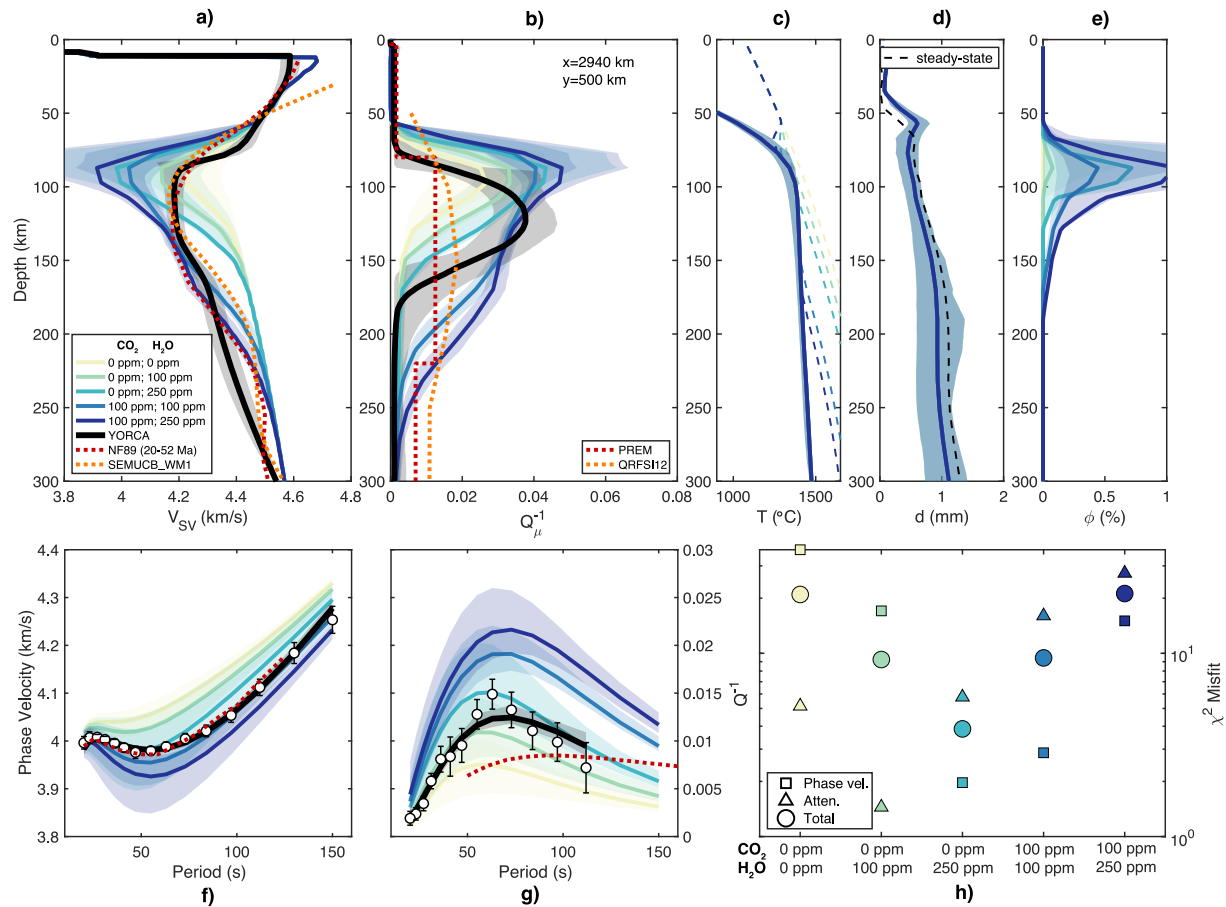
Figure 9. Spectral power of longitudinal structure in the non-adiabatic temperature versus depth at a plate age of 42 Ma in a depth range of 150–250 km, averaged over the periods of time where downwelling occurs. Since the y extent of the model is 1,000 km, the largest wavelength that can be present is 500 km. Models where no downwellings occur at 42 Ma plate age are not shown. The red horizontal line marks the wavelength of 250 km inferred from gravity undulations and body-wave tomography. For the distribution over time, see Figure S8 in Supporting Information S1.

Note that the analysis above is only for a plate age of 42 Ma and that both the temperature anomaly and frequency of cold downwellings are much higher for older plate ages (for 70 and 90 Ma, see Figures S4 and S5 in Supporting Information S1), where all of our models feature SSC. In this context it is worth noting that preliminary results from Old ORCA seem to show several more flurry-like downwellings, possibly with smaller non-adiabatic temperature excursions (Hariharan et al., 2024).

4.5. Evolution of the Best-Fit Model $1_{\text{diff}}/0.52_{\text{dis}}$

Figure 5 shows how SSC evolves in model $1_{\text{diff}}/0.52_{\text{dis}}$. Within the first ∼10 Myr, SSC initiates at all plate ages ≳35 Ma, and by 19 Myr (Figure 5 top left), the first downwellings have reached a depth of ∼300 km. While the morphology of these initial downwellings is still controlled by the random location of the initial temperature perturbations, the planform of convection shifts to longitudinal rolls at 30–35 Myr. At the same time, larger-scale convection cells in transverse direction develop as the initial downwellings break through the phase transition at 410 km depth (Figure 5 bottom left). This flow pattern represents a quasi-steady state that only changes slightly throughout the last 50 Myr of model evolution (Figure 5 bottom right). This model is also the only one to have

Figure 10. Comparison of seismic observations with VBRc calculations at $x = 2{,}940$ km, corresponding to ~42 Ma seafloor. Five different volatile cases are shown ranging from dry (0 ppm CO_2; 0 ppm H_2O) to wet (100 ppm CO_2; 250 ppm H_2O). (a) Shear velocity at Young ORCA (black) compared to regional model NF89 (Nishimura & Forsyth, 1989) in orange and global model SEMUCB_WM1 (French & Romanowicz, 2014) in red. (b) Same as (a) but for shear attenuation, where global model QRFSI12 (Dalton et al., 2008) is shown in orange. (c) Temperature (with solidi for each case shown by dashed lines) and (d) grain size from ASPECT are the same for all cases. (e) Melt fraction is calculated from the equilibrium hydrous melting model. (f) Rayleigh wave phase velocity and (g) attenuation observations (white symbols) at Young ORCA compared to the forward predictions from the models shown in (a) and (b), respectively. Shading indicates the middle 95% percentile of models for each case and 2σ uncertainties for observations. (h) Misfit for phase velocity, attenuation, and the combined average (total).

appreciable downwellings at plate ages of <40 Ma for appreciable fractions of model time, and some of these downwellings reach the transition zone (see Figure S3 in Supporting Information S1).

5. Fit to Seismological Observations

The primary seismological observations we seek to match by forward calculation ("translation") from the ASPECT model outputs are average shear velocity (V_S), average shear attenuation $\left(Q_\mu^{-1}\right)$, differential travel times, phase velocity and attenuation dispersion curves, and the amplitude and wavelength of tomographically imaged anomalies. Using the best-fit model described above (Section 4.5), we extract snapshots of the model for seismological forward calculations at a model time of 80 Myr, so chosen because these are times at which SSC at 42 Ma plate age appears vigorous based on the averaged temperature anomaly (Figure 8).

5.1. Surface-Wave Constraints: V_S and Q_μ

Surface wave observations at the Young ORCA experiment (Russell, 2021; Russell et al., 2023) help validate the geodynamic model by constraining the average physical state implied for the oceanic upper mantle, with shear velocity and attenuation sensitivity down to ~300 km depth. ASPECT model outputs are generally a good match with surface wave observations at Young ORCA (Figure 10). The magnitude of observed minimum V_{SV} and peak

Q_μ^{-1} (and associated minimum in phase velocity and peak in Rayleigh wave attenuation) fall within the range of values calculated for the volatile scenarios tested.

We first compare observations to predictions in the "data" space: dispersion curves of Rayleigh phase velocity and attenuation (Figures 10f and 10g). Although no single scenario fits all aspects of the observed data, we find overall lower misfit for the moderate volatile cases (Figure 10h) and the best total misfit for 250 ppm H_2O + 0 ppm CO_2. The low attenuation misfit for volatile-poor cases is primarily driven by the excellent fit to the (unattenuating) lithosphere at shorter periods <40 s. With increasing volatile content, attenuation misfit increases because both the amplitude and width of the attenuation peak become too large. The low phase velocity misfit for cases with high volatile content is primarily due to good fit at periods >80 s. At shorter periods (<40 s) sensitive to the lithosphere, the observations tend to favor the more volatile-poor models, whereas longer periods (>50 s) favor wetter models (Figure S6 in Supporting Information S1). These results would be consistent with an increase in volatile content with depth. In addition to the 80 Myr model time shown in Figure 10, we also tested a model time of 100 Myr and although it shows slightly lower velocities and higher attenuation in the asthenosphere (Figure S7 in Supporting Information S1), the pattern of data fits and main results remain unchanged.
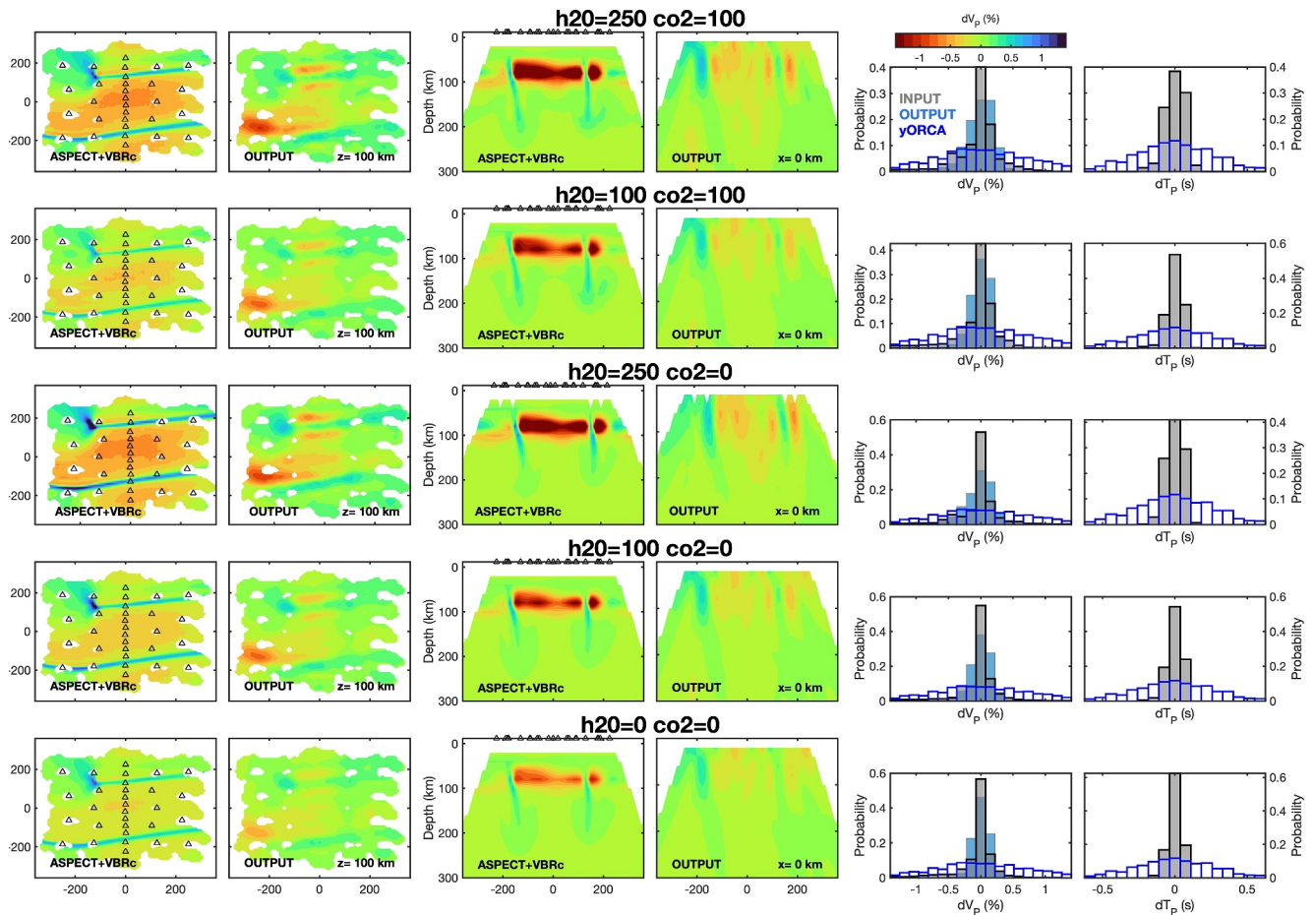
The difference between observed and calculated V_{SV} and Q_μ^{-1} profiles (the "model" space; Figures 10a and 10b) is more difficult to assess given that they are both affected by regularization and model parameterization choices. Nevertheless, there is decent agreement between the observed and calculated values that reflects the dispersion misfit discussed above. Perhaps the largest difference occurs in the low-velocity/high-attenuation zone beneath the plate, both of which are observed to be ~25 km deeper than predicted by the ASPECT outputs. In other words, the thermal lithosphere inferred by the seismic observations is thicker than that of the geodynamic model. This is unlikely to be a regularization issue because it can also be seen in the Rayleigh wave attenuation data; a thicker lithosphere is indicated in the observations by slightly weaker attenuation at periods <50 s and a peak at slightly longer periods compared to the volatile cases that best fit attenuation. The thicker seismic lithosphere could be the result of dehydration processes occurring at the mid-ocean ridge, if melt extraction removes volatiles from the lithosphere at depths of 60–120 km (Hirth & Kohlstedt, 1996) causing the solidus to steepen and increasing the depth at which the premelting effect is active. This has been invoked to explain the G discontinuity in the Pacific (Gaherty et al., 1999) as well as seismic anisotropy frozen into the Pacific lithosphere (Russell et al., 2019).

5.2. Body-Wave Constraints: δV_P (and δV_S)

One objective of this study was to evaluate the match between modeled SSC and 3-D structures observed in body wave tomography beneath the Young ORCA region (Eilon, Zhang, et al., 2022) and similarly elsewhere (H. Kang et al., 2023). Since these studies involve *differential* body wave measurements, they formally constrain only lateral variations in the elastic structure. We seek to match: (a) longitudinal planform of convective structure with elongation sub-parallel to plate motion; (b) longitudinal wavelength of ~200–300 km; (c) peak-to-peak differential P-wave arrival times of ~1 s; (d) peak-to-peak V_P contrast of up to 4%; (e) strongest anomaly depth of 200–300 km and weak anomalies in the 100–200 km depth range.

The "input" 3-D velocity models (i.e., translated from the ASPECT models) are distinctive for narrow sheets of high velocity downwelling material, embedded in relatively slow background mantle (Figure 11). In the best-fit model, the longitudinal separation of these sheets is of the order of 250 km (Figure 9), varying somewhat through model run time (Figure S8 in Supporting Information S1). These sheets are aligned sub-parallel to plate motion. Thus, observations (a) and (b) match well, which is unsurprising because these were among the criteria used to select the best-fit dynamical model.

Observations (c) and (d) are satisfied qualitatively but not quantitatively, in that the patterns of anomalies are matched, but not the amplitudes. The "input" models, reflecting the seismic predictions of the ASPECT models, contain approximately 2× smaller velocity variation than inferred from the true observations, and approximately 3× smaller differential travel times (Figure 11, right). Higher concentrations of volatiles yield larger contrast in model velocities, as the warmer parts of the model space allow for increasing potency of anelastic dissipation mechanisms activated by these volatiles (largely through premelting effects; Yamauchi & Takei, 2016) while the cold downwellings do not allow for these mechanisms and maintain high velocity. The values above reflect the most exaggerated volatile case, where we maximize the velocity contrast in the downwellings compared to surrounding mantle. The fastest model features have the greatest velocity contrast with their surroundings at their

Figure 11. Comparison of seismic velocity models for VBRc-translated ASPECT before and after ("OUTPUT") the tomographic inversion. Each row is a different case of volatiles, matching Figure 10. Left pair of columns are map-view at 100 km depth, with the locations of the synthetic OBS instruments shown as black triangles. Middle pair of columns are vertical sections at $x = 0$ looking toward negative x. Right columns are histograms of differential velocities (left; dV_P) and travel times (right; dT_P) with Young ORCA observations (Eilon, Zhang, et al., 2022) in blue and calculations from this analysis in gray (translated input) and blue (output, after the tomographic filter).

narrowest point, at ∼100 km depth, since here the cold temperatures are concentrated in a small volume and are contrasted with high homologous temperature ambient asthenosphere. At 150–250 km depth, these high velocity features spread out as they encounter resistance from increasing viscosity with depth (Section 4.4). However, although they slow at this depth, they also spread out laterally, and we do not observe volumetrically significant build-up of high velocity material, rather accumulation of material that is only moderately faster than ambient. As a result of the small volume of the fastest δV_P features, and the modest δV_P of the larger volume features, the predicted differential travel times (without noise added) are substantially smaller in amplitude compared to the δT_P observations (Figure 11). At a model time where the downwelling pattern is much more sheet-like, with one large downwelling dominating, the amplitude of computed heterogeneity from our model is somewhat closer to the observed value (Figure S9 in Supporting Information S1). However, the pattern of heterogeneity (a single principal velocity dichotomy between fast sheet and slow upwelling mantle) look quite different to our observed structure, so this explanation is unlikely to reconcile misfit in modeled versus observed heterogeneity amplitude.

The "output" models, with tomographic filter imposed, show several key differences with the input models. High-velocity features are muted and hard to identify in comparison to the input structures. The clearest features are actually low-relative-velocity structures. At depths greater than ∼100 km, almost no structure in the input models has absolute velocity lower than ambient. The broad low velocity features extending to ∼200 km depth in the "output" models reflect vertical downward smearing of shallow low velocity material (due to volatiles and melt) and the tomographic constraint that velocity averages to zero in horizontal layers. The extrema of velocity (both

fastest and slowest) are not recovered; there is overall amplitude reduction. As a result, the apples-to-apples match between the "output" seismic models and the observed tomography reveals an even more substantial undershoot in modeled heterogeneity. Moreover, as noted above observation (e) is not matched well, since the most substantial velocity heterogeneities (in both input and output models) are near the base of the plate, not strongest at 200–300 km depth. This is despite our having selected a model where the laterally averaged cold anomalies are in fact strongest at 200 and 300 km depth (as shown in Figure 7, red horizontal bars). Overall, the coarse features of the ORCA observations are matched by the model predictions, but the models fail to reproduce the amplitude of the apparent anomalies.

δV_S models were not obtained at Young ORCA, due to noisy horizontal channels preventing sufficient clean S-wave arrivals. We nevertheless computed synthetic S-wave tomography for completeness and for comparison with possible future shear-wavespeed studies (Figures S10 and S11 in Supporting Information S1). Unsurprisingly, these models are similar to their V_P counterparts but show larger velocity and travel time heterogeneity due to the stronger dependency of shear modulus on temperature, particularly considering shear anelasticity. For all but the volatile free case, we predict a relatively high $d \ln V_S/V_p$ ratio of 1.85–2.05 when averaging over all nodes in the well resolved portion of the sub-plate mantle.

6. Discussion

This study shows that it is possible to match coarse geophysical observations of the Young ORCA region with a dynamical model that includes SSC. In doing so, we require the asthenospheric viscosity in this region to be low (2×10^{19} Pa s)—commensurate with the strong attenuation—and determine that dislocation and diffusion creep act at similar rates just below the plate. This model is broadly consistent with: (a) Isostatic shallowing of the seafloor due to lithospheric thinning, and macroscopic thermal structure well-fit by a "plate cooling model"; (b) Elongated convective downwellings on a similar wavelength to satellite-imaged gravity rolls and seismically imaged velocity heterogeneities present at a plate age of ∼40 Ma; (c) Build-up of crystallographic fabrics and associated seismic anisotropy beneath the plates. With some assumptions about volatile concentrations in the asthenosphere, these models can also match observations of low phase velocities and high attenuation imaged by surface waves, with slowest velocities and highest dissipation in a narrow and presumably pervasive layer beneath the plate that must contain melt.

Although the fractions of melt required to match surface wave properties are modest (<0.7% for the best-fit scenario), this melt may be dynamically sustained over wide regions if, as our simulations suggest, SSC is a widespread process. Pervasive asthenospheric melt has previously been proposed from other geophysical constraints (Hua et al., 2023; Naif et al., 2013; Stern et al., 2015). If and when small fractions of this melt occasionally reach the surface, this could account for non-age-progressive, non-plume-sourced seamount volcanism observed sporadically but widely in the central oceans (Gevorgian et al., 2023; Koppers et al., 2003).

6.1. Do These Models Represent an Average Earth?

Our approach sought to test the plausibility of SSC beneath relatively young Pacific plate. The "best-fit" model described above should be interpreted in that context—as the model best fitting local geophysical constraints.

A central motivation for this work was to evaluate whether putative small scale convection could be the mechanism that leads to globally observed seafloor flattening with age. We find that indeed models with more vigorous SSC show marked seafloor flattening. While the temperature structure in our models is of course more complex than predicted for simple cooling, when we search for the best fit plate-cooling approximation to our average 2-D thermal structure in the vigorously convecting models, we obtain an equivalent "plate thickness" of 110 km (Figure 7) or a barely different 115 km at a later model snapshot (Figure S12 in Supporting Information S1). This value, which captures coarse thermal evolution, compares favorably to numerous published values for Earth's oceans (e.g., 125 ± 10 km in Parsons and Sclater (1977); 106 km in McKenzie et al. (2005); 95 ± 15 km in Stein and Stein (1992); 115 ± 5 km in Burgos et al. (2014); 135 ± 30 km in Richards et al. (2018)).

Importantly, although SSC in this model initiates at a seafloor age of ∼30 Ma, the departure between the model temperature structure and a best-fitting half-space cooling (HSC) prediction is not evident until ∼70 Ma (Figure 7, Figure S12 in Supporting Information S1), and the bathymetry accordingly does not depart from half-space

predictions (within uncertainty bounds) until much later than 40 Ma (Figure 6). That is to say, SSC initiating at earlier age than ∼70 Ma is plausibly consistent with observations of the seafloor depth–age curve.

Alternatively, even if our best-fit model does not represent the thermal evolution of an *average* oceanic plate, we may consider some subset of models in our test suite as plausible scenarios for plate evolution, depending on multiple heterogeneous properties including potential temperature and volatile concentrations (Dalton et al., 2014). Several prior studies have pointed out that Earth's limited inventory of oceanic lithosphere means that identification of any single "normal" plate evolution is challenging at best (e.g., Crosby et al., 2006; T. Korenaga & Korenaga, 2008). For instance, while the $1_{diff}/0.52_{dis}$ case applies best to Young ORCA, it may be that another model better describes average mantle. For instance, $10_{diff}/0.73_{dis}$ would more obviously reproduce a later onset of SSC, but have far smaller induced sub-plate heterogeneity and more subsidence than observed. Alternatively, an even lower viscosity model could better match observed shallowing. In this case, each model can be thought of as one streamline of plausible plate evolution. If so, the true average Earth comprises some weighted average of the model ensemble. This averaging is surely both intrinsic (diffusion of heat and chemistry smoothing out contrasts and plate strength suppressing short wavelength seafloor dynamics) and apparent (a limitation of short-wavelength sensitivity in oceanic geophysical data sets).

If Young ORCA plate and mantle are atypical, what does this mean for the physical state of the asthenosphere in this part of the central Pacific? Anomalously low viscosity may stem from excess mantle temperature or volatile concentrations. The Marquesas plume is only ∼750 km from the center of the Young ORCA array, and may contribute to hotter-than-average asthenosphere. Volatile-rich plumes rising from the deep mantle have elsewhere been postulated (Blatter et al., 2022; Dixon et al., 2008) to dampen and melt the asthenosphere. Alternatively, perhaps the Young ORCA plate is *typically* atypical. Widespread meso-scale thermal heterogeneity in the ocean basins from shallow or deep sources has previously been invoked to explain near-ubiquitous variability in asthenospheric velocity (Lei et al., 2020; Munch et al., 2024; Panet et al., 2024; Thrastarson et al., 2024) and in at least one global tomographic model Young ORCA sits on a flow-line that roughly tracks a low-velocity structure to the East Pacific Rise (French et al., 2013).

Although we have attempted to match the ∼250–300 km wavelength of periodic anomalies in gravity and seismic velocity at the Young ORCA site, this may not be appropriate for all sites with sublithospheric SSC. For instance, H. Kang et al. (2023) and Hariharan et al. (2024) observe large asthenospheric velocity contrasts beneath plate ages of 170 and 90 Ma, respectively, but imaged structure is not strongly linear or periodic and varies in a complex fashion with depth. Our simulations indicate that sublithospheric SSC can take many planforms, and the most vigorous downwellings are often spoke-patterned. Particularly at the onsets of instabilities, we find flurries of blob-like downwellings trailed by thin vertical channels. The simulations are therefore consistent with the possibility that SSC may produce upper mantle velocity heterogeneity with various morphologies.

6.2. Impact of a Variable Grain Size on SSC Dynamics and Asthenosphere Properties

Constraints on grain size evolution were a primary motivation for this study. We do observe large variations in dynamics between model simulations that result in different grain sizes, suggesting that grain size plays some role in the expression of SSC. However, we find that grain sizes beneath the plate do not vary greatly in our best-fit model (0.2–1.5 mm in the upper 300 km). Grain size has been invoked as a factor that may exaggerate anelastic effects beneath the oceanic plate (Faul & Jackson, 2005; Russell et al., 2023), but in our simulations grain sizes are relatively large in the volumetrically dominant regions between downwellings, where the mantle is warmer and more slowly deforming. By contrast, within the downwellings, high strain rates and slow grain growth reduce the grain size, acting in opposition to the temperature effect by making downwelling regions seismically slower and more dissipative. This mutes the wavespeed contrast between downwellings and their surroundings.

6.2.1. Grain Size Evolution Parameters

Several of our model assumptions influence how grain size (and the resulting wavespeed) within downwellings differs from the surrounding mantle. Our model does not account for the presence of volatiles or melt, and thus features moderately fast grain growth, resulting in grain sizes of the order 0.5–1 mm (see Figure 10). Behn et al. (2009), who assume wet olivine for their grain growth and rheologic laws, predict substantially larger grain sizes (5–20 mm at ∼150 km depth, increasing to 20–30 mm at 400 km depth). Their model achieves a good fit to

previous 1-D shear velocity profiles, but does not match the strong and relatively sharp peak in shear attenuation (and minimum in shear velocity) that is observed at Young ORCA.

In the mantle, we expect spatial variations in volatile content, since volatiles are extracted from the lithosphere during mid-ocean ridge melting (e.g., Hirth & Kohlstedt, 1996) while the asthenosphere may be hydrated by plumes (e.g., Blatter et al., 2022). Overall, we expect the plate to be dry compared to the underlying asthenosphere. Under this assumption, grain growth should be faster in the warmer, wetter zones between downwellings, even further muting the contrast in seismic wavespeed.

The rate of grain size reduction is also uncertain. We assumed that the fraction of mechanical work done by dislocation creep that goes into reducing the grain size is constant at 10%. However, it has been suggested that this partitioning is temperature-dependent (Rozel et al., 2011), with much lower work fractions for higher temperatures. If true, this would make grain size reduction and strain localization at the base of the lithosphere and around the downwellings less efficient. If the cold downwellings have more efficient conversion of mechanical work to grain boundary energy (leading to smaller grains) this could be yet one more factor that mutes the seismological contrast between the downwellings and their surroundings (the opposite of what observations suggest).

6.2.2. Sub-Plate Flow Regime

The asthenospheric flow regime (Couette vs. Poiseuille) can impact profiles of grain size, and therefore viscosity (Ramirez et al., 2023). For the endmember of Couette flow, driven by the shear stress imposed by movement of the plate over passive asthenosphere, the strongest deformation occurs at the depth with the lowest viscosity (and for constant viscosity, velocity changes with depth linearly). By contrast, Poiseuille flow (or "plug flow") is driven by a sub-plate pressure gradient, so that the velocity distribution is parabolic for a constant viscosity, with the largest deformation at the top and bottom of the asthenosphere.

Our models assume Couette flow, since we do not know what the lateral pressure gradients in the asthenosphere might be. However, a significant component of Poiseuille flow, contributing at least 50% of the plate driving force, has been argued for the Pacific (Semple & Lenardic, 2018, 2020; Stotz et al., 2018). This might lead to certain behavior not captured by our models, such as physical segregation of strain rate between a large grain size, high viscosity, non-deforming plug (Ramirez et al., 2023) and localized high strain above and below, including a weak asthenosphere (the upper strain rate gradient). This would reduce asthenospheric grain size and lead to a positive feedback of strain rate concentration. Cold downwellings could then move more quickly through the low viscosity asthenosphere and gather near the top of the large grain size region caused by the undeforming plug, producing broader wavespeed anomalies at deeper depths, as observed in the body-wave tomography (Eilon, Zhang, et al., 2022). Smaller grain sizes would also reduce permeability within the asthenosphere, potentially allowing <0.7% partial melt to remain trapped. At the bottom of the plug (potentially in the mantle transition zone), strong deformation would also cause grain size reduction (Ramirez et al., 2023), but existing surface wave attenuation observations do not have the depth sensitivity to resolve this. Note also that our work suggests that large grain sizes within the plug predicted by 1D models such as Ramirez et al. (2023) would likely be smaller in a 3D mantle with more complex deformation patterns.

Either Couette or Poiseuille flow in the olivine-rich upper mantle should lead to formation of a lattice-preferred orientation (LPO) and seismic anisotropy (Zhang & Karato, 1995). This has been widely observed in the Pacific upper mantle (Eddy et al., 2022; Kawano et al., 2023; Lin et al., 2016; Montagner & Nataf, 1986; Nishimura & Forsyth, 1989; Raitt et al., 1969; Russell et al., 2019, 2022; Takeo et al., 2013, 2014, 2016, 2018), where asthenospheric fabric seems mostly horizontal and aligned approximately parallel to absolute plate motion (Becker et al., 2014). In contrast, SSC involves primarily vertical flow, which may modify the coherent horizontal fabric (Lin et al., 2016). Numerical flow models combined with forward calculations of LPO and seismic anisotropy indicate that SSC can reduce seismic anisotropy by ∼2% on average and can perturb the fast orientation by <20° beneath old lithosphere, but the broad-scale pattern of LPO remains largely aligned parallel to plate motion (van Hunen & Čadek, 2009). Indeed, Rayleigh waves show a reduction in seismic anisotropy with seafloor age in the Pacific (Eddy et al., 2019), consistent with this notion of SSC-perturbed fabric.

In our models, SSC often appears as flurries of vertical downwellings, which are transient in nature and move quickly through the low viscosity asthenosphere, and thus might not significantly perturb the overall horizontal

fabric. This is especially true given that in our models the volumetric majority of the asthenosphere is undergoing horizontal shear at any moment in time. This may explain why, at Young ORCA, shear-wave anisotropy is complex but not obviously affected by SSC. Within the plate, azimuthal anisotropy is strong (∼3%) and parallel to fossil spreading. Beneath the plate, it slightly weakens by ∼0.5% and fast directions rotate toward absolute plate motion between ∼90–170 km depth. Below this, fast azimuths rotate away from plate motion (and strength further weakens), consistent with deeper flow beneath the plate that is oriented in a different direction (Russell, 2021).

6.3. Reconciling and Interpreting Disagreements Between Seismological Predictions and Observations

We evaluate mismatches between our simulations and real-world seismological observations (Section 5.2) in three connected categories: observable data (e.g., differential travel times and phase velocity), inverted seismological properties and structure (e.g., velocity contrast, absolute velocity, attenuation), and underlying state variables (e.g., the true temperature range).

6.3.1. Differences in Observable Data

Even if our modeled seismic properties exactly matched the Earth, seismological measurements provide only an imperfect snapshot of those properties. Surface wave phase velocity measurements are inherently sensitive to large volumes of the upper mantle, yet dynamical models show fine-scale structure, including thin downwellings separated by broad updrafts. Surface waves might primarily capture the latter, biasing observations away from the colder mantle regions. With regard to body waves, the spread in observed differential travel times far exceeds the predictions (Figure 11), implying much greater velocity heterogeneity. This misfit cannot be explained as a consequence of limited tomographic resolution. However, this misfit may, in part, owe to noise. OBS stations are notoriously noise-prone. The effects of noise can be conceptualized as convolving a Gaussian noise PDF with the "true" data PDF, yielding a broader "observed" data distribution, more in line with observations. If this noise were truly stochastic, then it should not alter the output tomographic models. Note that OBS stations may also have idiosyncratic sources of measurement error, such as clock drift (Cabieces et al., 2024), though Young ORCA instruments were theoretically corrected for this effect (Eilon, Gaherty, et al., 2022).

6.3.2. Differences in Seismological Properties

In tomographic model space, we see a mismatch between large observed δV_P from Eilon, Zhang, et al. (2022) and the dynamic models' smaller "input" velocity heterogeneity, let alone the more muted "output" models (Figure 11). The "observed" velocity contrasts are the outputs of a tomographic inversion. If that inversion were under-regularized then it might exaggerate true heterogeneity. Hariharan et al. (2024) show that defensible regularization choices can alter apparent temperature contrast by as much as a 100 K, with relatively little change in data fit. That said, most body wave inversions suffer from the opposite problem: synthetic recovery tests usually reveal amplitude loss in the inversion. Another mismatch is that predicted velocity contrasts are maximal at shallow depths (70–150 km, where downwellings descend through warm asthenosphere) whereas observations indicate deeper maximum velocity contrasts (180–280 km). However, this type of tomography is susceptible to vertical smearing, and Eilon, Zhang, et al. (2022) showed that while this deeper depth range is preferred by the data, a shallower range did not enormously worsen the weighted variance reduction. For surface waves, we only interpret 1-D profiles that average over the entire array footprint (Figure 10), thus 3-D heterogeneity is ignored. The averaging and inversion of real surface-wave dispersion data to obtain 1-D profiles homogenizes details of the true structure. We have attempted to mimic this behavior by averaging the "translated" 1-D profiles over the footprint of the ORCA array. However, subtle differences between observations and dynamic model predictions may be attributed to the different strategies used to obtain 1-D profiles.

Another possibility is that our "translations" underestimate true δV contrast. In the sub-plate mantle (temperatures >1150℃, which includes most of our drips) we assumed bulk volatiles are uniformly distributed (though we do account for partitioning out of the solid phase if melt is present). This assumption may be wrong. Melting and dehydration at the ridge (Plank & Langmuir, 1992) should deplete the portion of the mantle that will become lower oceanic lithosphere, relative to a much more volatile-rich oceanic asthenosphere (somewhere between average MOR-source (Hirth & Kohlstedt, 1996) and a plume-enriched endmember (Blatter et al., 2022; Dixon et al., 2008)). If, in the real Earth, dry lower lithosphere drips into more wet and/or carbonated asthenosphere, then

differential activation of anelastic mechanisms and (pre-)melting could exaggerate seismological contrasts (Dasgupta & Hirschmann, 2010; Hirschmann, 2006; Yamauchi & Takei, 2024).

Alternatively, our translation approach might wholly miss some important factors, such as melting of fertile pockets or mixed-in basalt (Morgan & Morgan, 2024), oxygen fugacity (L. Kang & Karato, 2023), composition, or an un-parameterized anelastic mechanism (Olugboji et al., 2013). Any of these could exaggerate velocity contrast and, depending on the physical distribution of the underlying cause, could also explain why the observed maximal contrast appears to be deeper within the asthenosphere than modeled.

Finally, this study sheds light on a perplexing feature of some body-wave derived SSC images in the oceans: the preponderance of slow imaged anomalies (Eilon, Zhang, et al., 2022; Hariharan et al., 2024; H. Kang et al., 2023). These appear to confound expectations of top-driven convection, which entails cold (fast absolute velocity) material dropping into ambient (average absolute velocity) mantle, perhaps with some melt (modestly slow absolute velocity). The extent to which imaged velocity contrasts indicate unusually hot, cold, or molten material in the asthenosphere is a topic of debate (Hariharan et al., 2024). Our synthetic tomography reveals that the tomographic filter may exaggerate the presence and amplitude of the relatively slow structures (Figure 11). The upshot is that body wave observations that include large apparently slow features are consistent with top-driven SSC at a cold thermal boundary layer.

6.3.3. Differences in Underlying State Variables

If we assume that observed models are not far wrong, and nothing profound is incorrect about our state-variable-to-velocity scaling, then a fundamental challenge in reconciling seismic observations and our dynamic model outputs are the extremely cold ($\Delta T < -200$ K) downwellings required to explain high observed velocity contrasts. In the following, we discuss complexities not captured in our models that could lead them to underestimate the wavespeed anomalies associated with the downwellings.

We do not take into account any heterogeneities in the ridge-parallel direction, such as fracture zones and the corresponding change in plate age. While there are no fracture zones crossing through the Young ORCA array, both the Marquesas Fracture Zone to the south and the Galapagos Fracture Zone to the north might affect convective flow, as might smaller-scale offsets in the MOR between these large transforms. Past modeling studies (Dumoulin et al., 2005; Huang et al., 2003) have shown that plate-age offsets at fracture zones can facilitate SSC at younger plate ages, where its onset then occurs near the fracture zone. Eilon, Gaherty, et al. (2022) document a band of rotated abyssal hill fabric through the center of this field region consistent with the "wake" of an overlapping spreading center (e.g., Macdonald et al., 1987) that might indicate along-strike segmentation in the formative MOR.

The nearby Marquesas plume might influence SSC below Young ORCA, both through its effect on mantle flow (see discussion on Couette vs. Poiseuille flow in Section 6.2.2) and through the associated increase in mantle temperature. If the asthenosphere has a higher potential temperature than assumed in our models, both the stronger temperature contrast with the lithosphere and the additional generation of melt would result in a larger contrast in seismic velocities, potentially better matching the seismic body-wave observations. The impact of the melting process itself has been shown to be complex (Ballmer et al., 2009, 2011), either enhancing or delaying SSC (Agrusta et al., 2015), since it can make the upwellings either more buoyant (because depleted mantle is less dense) or less buoyant (due to cooling from latent heat consumption upon melting). Taken together, these simplifications could contribute to modeled cold downwelling s being too small in terms of their size and/or temperature anomaly. This might help explain our mismatch to seismic wavespeed contrast and travel times (Section 5.2).

The two main parameters controlling SSC onset and morphology are the Rayleigh number (Ra) and the temperature-dependence of viscosity (Section 4.2). The stronger the temperature-dependence, the thinner the layer that can participate in convective instability (see for example, Conrad & Molnar, 1999; Davaille & Jaupart, 1994). Therefore, a higher activation energy (at a given Ra) means there is less buoyancy available for the cold downwellings to form, so they develop later and remove less material, making them smaller in size and in terms of their temperature (and seismic) anomaly. We took the activation energy from Hirth and Kohlstedt (2003): 375 ± 50 kJ/mol for dry diffusion creep (± 75 kJ/mol if wet). Experimental uncertainty therefore allows for substantially lower values of E_{diff}. Additionally, if the work fraction reducing the grain size is temperature-

dependent as outlined above, grain size would be reduced more efficiently within the colder lithosphere compared to the hotter asthenosphere below, leading to a stronger grain size contrast between the two. Both effects would allow for more of the cold lithosphere to become unstable and participate in the downwellings, making them colder and larger. However, a lower activation energy and therefore thicker layer of convective instability also leads to earlier onset and larger wavelength of SSC (Conrad & Molnar, 1999). Keeping the onset time at 30–40 Ma plate age would then require an asthenosphere with lower *Ra*, also associated with a larger characteristic length scale of flow (see Figure 9). In addition, if enough cold material were to be removed from the plate at 40–45 Ma plate age to create downwellings with an amplitude of $\Delta T > 200$ K as suggested by body wave observations (Eilon, Zhang, et al., 2022), there should be a more visible signal in the seafloor topography (and possibly heat flux). Therefore, it is challenging to find a mechanism that would both explain the observed short wavelength and the large amplitude of the convection rolls at 42 Ma plate age, while also being consistent with the other observations.

Other than the amplitude of the drips' temperature anomaly, a larger volume of cold material could also produce large travel time contrasts. While drips' individual volume is limited by factors described above, a long-term accumulation of cold material at 250–350 km depth could lead to a better match with the seismic observables. Due to the increase in viscosity with depth, downwellings in our models stall for a few Myr to a few tens of Myr before breaking through into the transition zone. This phenomenon was proposed by Eilon, Zhang, et al. (2022) as an explanation for the large observed fast wavespeed anomalies. Several factors could contribute to increasing this time scale. Examples are a larger viscosity increase at 410 km depth, or upwards mantle flow, perhaps related to the nearby Marquesas plume or the Pacific LLSVP. Furthermore, if there was a component of mantle flow in the opposite direction of plate motion, cold drips could be translated beneath a slightly younger part of the plate than where they originated from. Such downwellings, sourced from a plate that had more time to cool, could therefore potentially be larger despite appearing beneath the younger aged plate.

Seismic imaging provides a snapshot in time. Yet, modeled SSC shows both spatial and temporal fluctuations. This may be another reason for synthetic and true structure not clearly matching—we may not be comparing "apples-to-apples." We did attempt to evaluate comparable structure by using a snapshot in model time that corresponds to substantial downwellings at ∼40 Ma and by placing our artificial seismic array at the age corresponding to young ORCA (42 Ma). But models show structures evolving quickly, the ridge-parallel position of the array is arbitrary (we selected a location with clear downwellings within the array footprint), and we find that most of the array lies within the "stable" longitudinal downwelling cells, which have smaller depth extent than the main downwellings. Models (Figure 8 and Movies S2 and S3) indicate that the largest temperature excursions are at the onsets of downwellings. If Young ORCA happens to truly sit atop a nascent downwelling, the temperature contrast would be higher than estimated in our snapshots that mostly contain tails of mature downwellings. In this context it is worth noting that other OBS-based tomographic studies have inferred much larger (500–1,100 K in H. Kang et al., 2023) or more modest (∼70 K in Hariharan et al., 2024) temperature contrasts in apparent convective cells beneath even older seafloor.

6.3.4. Challenges Converting Geodynamic Models to Seismic Observables

It is not straightforward to convert state variables output from geodynamic simulations into seismic properties that can be directly compared with observations. Decisions must be made along the way, such as which laboratory scaling relationship(s) to use, the appropriate frequency at which to calculate anelastic effects, how melt and volatiles are handled (if at all), and how these effects will be incorporated in a way that remains somewhat self-consistent with the geodynamic modeling. This last point is particularly challenging with regard to the impact of melt and volatiles on effective viscosity. The different flow law prefactors tested in the dynamic models can represent the weakening effect resulting from different bulk mantle hydration states, but solidus depression additionally reduces diffusion viscosity through the premelt effect (and generation of melt) in the translated models. Adding the effects of volatiles and melt in post-processing, as we have done here, implies viscosities that are lower than those output from the geodynamic simulations (Figure S1 in Supporting Information S1). Even in a melt-free and dry case, the premelting effect reduces the diffusion creep viscosity (Yamauchi & Takei, 2016), potentially reducing the overall effective viscosity and changing the relative rates of diffusion and dislocation creep. This apparent inconsistency between the rheology of the dynamical modeling and that of the output seismic

conversion is inherent and cannot be removed by simply tweaking viscosity prefactors or other parameters. Future models that couple the effects of melt and volatiles directly into the dynamics will help resolve this inconsistency, but for now, we simply acknowledge the limitation. That we are able to approximately fit seismic attenuation with a reduced viscosity relative to the geodynamic model would suggest that either viscosity should be even lower in the simulations (which would misfit other observations) or some unaccounted for phenomenon enhances attenuation without reducing viscosity.

7. Conclusions

In this study, we conducted high-resolution 3D geodynamic modeling of an aging oceanic lithosphere–asthenosphere system, incorporating a composite diffusion/dislocation creep rheology with dynamically evolving grain size. We tested a variety of possible mantle viscosity scenarios by systematically changing the combinations of flow law prefactors to vary both absolute viscosity and the dominant creep mechanism. All of these models feature small-scale sub-lithospheric convection (SSC), with the age of onset depending on the viscosity structure. We determined that SSC can be a significant process for adding heat to the base of the plates. Initial downwellings quickly align into longitudinal "rolls," but over time an additional transverse component of the convective cells develops, with flurries of more spoke-like instabilities typically clustering at periodic spacing corresponding to their build-up time. To identify the scenario that most plausibly replicates a site on Earth, we compared the thermal structure and grain size distribution in these models to seismological observations of SSC in the central Pacific Ocean, including beneath relatively young (42 Ma) plate age at the Young ORCA array. Specifically, we sought to match the wavelength and pattern of observed longitudinal convective rolls, and to reconcile model predictions with measurements of large seismic velocity heterogeneity, low absolute seismic velocities, and high seismic attenuation. On the basis of predominance of upper mantle dislocation creep (concordant with globally observed seismic anisotropy), early onset of SSC instability (matching seismic observations), and maximal amplitude and appropriate wavelength of temperature heterogeneity, we select a particular model, "$1_{diff}/0.52_{dis}$," as the best-fit dynamical model that may represent Young ORCA dynamics. A key feature required to match the observations is a low ($< 2 \times 10^{19}$ Pa s) asthenospheric viscosity, and both diffusion and dislocation creep are important drivers of deformation. Additionally, the increase in viscosity with depth slows down cold downwellings in the upper mantle so that negative temperature anomalies can accumulate in a depth range of 200–300 km. SSC in this model (as with some others) removes cold material from the base of the plate in a fashion that leads to a temperature structure closely resembling a plate cooling model (with a best-fitting plate thickness of 110 km). The associated flattening of the seafloor depth–age curve, most evident beyond ~60 Ma, approximately matches global observations, providing potential evidence for this type of vigorous oceanic SSC playing a key role in Earth's plate dynamics. Although our models do not include the effects of melt or volatiles, we find that some amount of both is required to match observed asthenospheric low seismic velocities and high attenuation, given the temperatures and grain sizes predicted by the models. Even with these factors accounted for, it is challenging to reconcile all the seismological observations. In particular, the amplitude and/or volume of high and low velocity seismic heterogeneities suggested by body wave tomography does not match the structures in our dynamical models. Our results therefore suggest that some additional mechanism allowing for larger/colder/faster downwellings or seismically slower upwellings must be at play. In the future, this work could be extended by incorporating melt and volatile dynamics in the simulations, as well as the explorations of poorly constrained grain growth parameters.

Data Availability Statement

References

Abers, G. A., Fischer, K. M., Hirth, G., Wiens, D. A., Plank, T., Holtzman, B. K., et al. (2014). Reconciling mantle attenuation-temperature relationships from seismology, petrology, and laboratory measurements. *Geochemistry, Geophysics, Geosystems*, *15*(9), 3521–3542. https://doi.org/10.1002/2014GC005444

Agrusta, R., Tommasi, A., Arcay, D., Gonzalez, A., & Gerya, T. (2015). How partial melting affects small-scale convection in a plume-fed sublithospheric layer beneath fast-moving plates. *Geochemistry, Geophysics, Geosystems*, *16*(11), 3924–3945. https://doi.org/10.1002/2015gc005967

Austin, N. J., & Evans, B. (2007). Paleowattmeters: A scaling relation for dynamically recrystallized grain size. *Geology*, *35*(4), 343. https://doi.org/10.1130/G23244A.1

Ballmer, M. D., Ito, G., van Hunen, J., & Tackley, P. J. (2010). Small-scale sublithospheric convection reconciles geochemistry and geochronology of "Superplume" volcanism in the western and south Pacific. *Earth and Planetary Science Letters*, *290*(1–2), 224–232. https://doi.org/10.1016/j.epsl.2009.12.025

Ballmer, M. D., Ito, G., Van Hunen, J., & Tackley, P. J. (2011). Spatial and temporal variability in Hawaiian hotspot volcanism induced by small-scale convection. *Nature Geoscience*, *4*(7), 457–460. https://doi.org/10.1038/ngeo1187

Ballmer, M. D., van Hunen, J., Ito, G., Bianco, T. A., & Tackley, P. J. (2009). Intraplate volcanism with complex age-distance patterns: A case for small-scale sublithospheric convection. *Geochemistry, Geophysics, Geosystems*, *10*(6), Q06015. https://doi.org/10.1029/2009GC002386

Ballmer, M. D., van Hunen, J., Ito, G., Tackley, P. J., & Bianco, T. A. (2007). Non-hotspot volcano chains originating from small-scale sublithospheric convection. *Geophysical Research Letters*, *34*(23), L23310. https://doi.org/10.1029/2007GL031636

Bangerth, W., Dannberg, J., Fraters, M., Gassmoeller, R., Glerum, A., Heister, T., et al. (2023). Aspect v2.5.0. *Zenodo*. https://doi.org/10.5281/zenodo.8200213

Becker, T. W., Conrad, C. P., Schaeffer, A. J., & Lebedev, S. (2014). Origin of azimuthal seismic anisotropy in oceanic plates and mantle. *Earth and Planetary Science Letters*, *401*, 236–250. https://doi.org/10.1016/j.epsl.2014.06.014

Behn, M. D., Hirth, G., & Elsenbeck, J. R., II. (2009). Implications of grain size evolution on the seismic structure of the oceanic upper mantle. *Earth and Planetary Science Letters*, *282*(1–4), 178–189. https://doi.org/10.1016/j.epsl.2009.03.014

Blatter, D., Naif, S., Key, K., & Ray, A. (2022). A plume origin for hydrous melt at the lithosphere–asthenosphere boundary. *Nature*, *604*(7906), 491–494. https://doi.org/10.1038/s41586-022-04483-w

Brunsvik, B. R., Eilon, Z. C., & Lynner, C. (2021). Mantle structure and flow across the continent-ocean transition of the eastern North American margin: Anisotropic *S*-wave tomography. *Geochemistry, Geophysics, Geosystems*, *22*(12), e2021GC010084. https://doi.org/10.1029/2021GC010084

Buck, W. R. (1986). Small-scale convection induced by passive rifting: The cause for uplift of rift shoulders. *Earth and Planetary Science Letters*, *77*(3–4), 362–372. https://doi.org/10.1016/0012-821X(86)90146-9

Buck, W. R., & Parmentier, E. M. (1986). Convection beneath young oceanic lithosphere: Implications for thermal structure and gravity. *Journal of Geophysical Research: Solid Earth*, *91*(B2), 1961–1974. https://doi.org/10.1029/jb091ib02p01961

Burgos, G., Montagner, J.-P., Beucler, E., Capdeville, Y., Mocquet, A., & Drilleau, M. (2014). Oceanic lithosphere-asthenosphere boundary from surface wave dispersion data. *Journal of Geophysical Research: Solid Earth*, *119*(2), 1079–1093. https://doi.org/10.1002/2013JB010528

Burke, J. E. (1949). *Grain control in industrial metallurgy*. American Society for Metals.

Cabieces, R., Harris, K., Ferreira, A. M. G., Tsekhmistrenko, M., Hicks, S. P., KrÃŒger, F., et al. (2024). Clock drift corrections for large aperture ocean bottom seismometer arrays: Application to the UPFLOW array in the mid-Atlantic Ocean. *Geophysical Journal International*, *239*(3), 1709–1728. https://doi.org/10.1093/gji/ggae354

Choblet, G., & Sotin, C. (2000). 3d thermal convection with variable viscosity: Can transient cooling be described by a quasi-static scaling law? *Physics of the Earth and Planetary Interiors*, *119*(3–4), 321–336. https://doi.org/10.1016/s0031-9201(00)00136-9

Connolly, J. (2005). Computation of phase equilibria by linear programming: A tool for geodynamic modeling and its application to subduction zone decarbonation. *Earth and Planetary Science Letters*, *236*(1–2), 524–541. https://doi.org/10.1016/j.epsl.2005.04.033

Connolly, J., & Kerrick, D. (1987). An algorithm and computer program for calculating composition phase diagrams. *Calphad*, *11*(1), 1–55. https://doi.org/10.1016/0364-5916(87)90018-6

Conrad, C. P., & Molnar, P. (1999). Convective instability of a boundary layer with temperature-and strain-rate-dependent viscosity in terms of "available buoyancy". *Geophysical Journal International*, *139*(1), 51–68. https://doi.org/10.1046/j.1365-246X.1999.00896.x

Crosby, A. G., McKenzie, D., & Sclater, J. G. (2006). The relationship between depth, age and gravity in the oceans. *Geophysical Journal International*, *166*(2), 553–573. https://doi.org/10.1111/j.1365-246X.2006.03015.x

Dalton, C. A., Ekström, G., & Dziewoński, A. M. (2008). The global attenuation structure of the upper mantle. *Journal of Geophysical Research*, *113*(B9), B09303. https://doi.org/10.1029/2007jb005429

Dalton, C. A., Langmuir, C. H., & Gale, A. (2014). Geophysical and geochemical evidence for deep temperature variations beneath mid-ocean ridges. *Science*, *344*(6179), 80–83. https://doi.org/10.1126/science.1249466

Dannberg, J., Eilon, Z., Faul, U., Gassmöller, R., Moulik, P., & Myhill, R. (2017). The importance of grain size to mantle dynamics and seismological observations. *Geochemistry, Geophysics, Geosystems*, *18*(8), 3034–3061. https://doi.org/10.1002/2017gc006944

Dannberg, J., Eilon, Z., Russell, J. B., & Gassmoeller, R. (2025). Understanding sub-lithospheric small-scale convection by linking models of grain size evolution, mantle convection and seismic tomography: Data. *Zenodo*. https://doi.org/10.5281/zenodo.14916284

Dasgupta, R., & Hirschmann, M. M. (2010). The deep carbon cycle and melting in Earth's interior. *Earth and Planetary Science Letters*, *298*(1–2), 1–13. https://doi.org/10.1016/j.epsl.2010.06.039

Dasgupta, R., Hirschmann, M. M., & Smith, N. D. (2007). Water follows carbon: CO_2 incites deep silicate melting and dehydration beneath mid-ocean ridges. *Geology*, *35*(2), 135. https://doi.org/10.1130/G22856A.1

Dasgupta, R., Mallik, A., Tsuno, K., Withers, A. C., Hirth, G., & Hirschmann, M. M. (2013). Carbon-dioxide-rich silicate melt in the Earth's upper mantle. *Nature*, *493*(7431), 211–215. https://doi.org/10.1038/nature11731

Davaille, A., & Jaupart, C. (1993). Transient high-Rayleigh-number thermal convection with large viscosity variations. *Journal of Fluid Mechanics*, *253*, 141–166. https://doi.org/10.1017/s0022112093001740

Davaille, A., & Jaupart, C. (1994). Onset of thermal convection in fluids with temperature-dependent viscosity: Application to the oceanic mantle. *Journal of Geophysical Research*, *99*(B10), 19853–19866. https://doi.org/10.1029/94jb01405

Dixon, J., Clague, D. A., Cousens, B., Monsalve, M. L., & Uhl, J. (2008). Carbonatite and silicate melt metasomatism of the mantle surrounding the Hawaiian plume: Evidence from volatiles, trace elements, and radiogenic isotopes in rejuvenated-stage lavas from Niihau, Hawaii. *Geochemistry, Geophysics, Geosystems*, *9*(9), Q09005. https://doi.org/10.1029/2008GC002076

Dumoulin, C., Doin, M.-P., Arcay, D., & Fleitout, L. (2005). Onset of small-scale instabilities at the base of the lithosphere: Scaling laws and role of pre-existing lithospheric structures. *Geophysical Journal International*, *160*(1), 344–356. https://doi.org/10.1111/j.1365-246x.2004.02475.x

Eddy, C. L., Ekström, G., & Nettles, M. (2022). Three-dimensional seismic anisotropy in the Pacific upper mantle from inversion of a surface-wave dispersion data set. *Geophysical Journal International*, *231*(1), 355–383. https://doi.org/10.1093/gji/ggac194

Eddy, C. L., Ekström, G., Nettles, M., & Gaherty, J. B. (2019). Age dependence and anisotropy of surface-wave phase velocities in the Pacific. *Geophysical Journal International*, *216*(1), 640–658. https://doi.org/10.1093/gji/ggy438

Eilon, Z. C., Gaherty, J. B., Zhang, L., Russell, J. B., McPeak, S., Phillips, J., et al. (2022). The Pacific OBS research into convecting asthenosphere (ORCA) experiment. *Seismological Research Letters*, *93*(1), 477–493. https://doi.org/10.1785/0220210173

Eilon, Z. C., Zhang, L., Gaherty, J. B., Forsyth, D. W., & Russell, J. B. (2022). Sub-lithospheric small-scale convection tomographically imaged beneath the Pacific plate. *Geophysical Research Letters*, *49*(18), e2022GL100351. https://doi.org/10.1029/2022GL100351

Faul, U., & Jackson, I. (2005). The seismological signature of temperature and grain size variations in the upper mantle. *Earth and Planetary Science Letters*, *234*, 119–134. https://doi.org/10.1029/2001jb001225

Faul, U., & Jackson, I. (2015). Transient creep and strain energy dissipation: An experimental perspective. *Annual Review of Earth and Planetary Sciences*, *43*(1), 541–569. https://doi.org/10.1146/annurev-earth-060313-054732

French, S., Lekic, V., Romanowicz, B., Shekhawat, A., Alemi, A. A., McEuen, P. L., et al. (2013). Waveform tomography reveals channeled flow at the base of the oceanic asthenosphere. *Science*, *342*(6155), 224–227. https://doi.org/10.1126/science.1242248

French, S., & Romanowicz, B. A. (2014). Whole-mantle radially anisotropic shear velocity structure from spectral-element waveform tomography. *Geophysical Journal International*, *199*(3), 1303–1327. https://doi.org/10.1093/gji/ggu334

Gaherty, J. B., Kato, M., & Jordan, T. H. (1999). Seismological structure of the upper mantle: A regional comparison of seismic layering. *Physics of the Earth and Planetary Interiors*, *110*(1–2), 21–41. https://doi.org/10.1016/S0031-9201(98)00132-0

Gevorgian, J., Sandwell, D. T., Yu, Y., Kim, S., & Wessel, P. (2023). Global distribution and morphology of small seamounts. *Earth and Space Science*, *10*(4), e2022EA002331. https://doi.org/10.1029/2022EA002331

Hall, C. E., & Parmentier, E. (2003). Influence of grain size evolution on convective instability. *Geochemistry, Geophysics, Geosystems*, *4*(3), 1029. https://doi.org/10.1029/2002gc000308

Hariharan, A., Eilon, Z., Gaherty, J. B., Forsyth, D. W., Russell, J., & Phillips, J. (2024). New observations of small-scale mantle heterogeneity beneath 90 Ma oceanic lithosphere. Washington, D. C.

Harmon, N., Forsyth, D. W., Weeraratne, D. S., Yang, Y., & Webb, S. C. (2011). Mantle heterogeneity and off axis volcanism on young Pacific lithosphere. *Earth and Planetary Science Letters*, *311*(3–4), 306–315. https://doi.org/10.1016/j.epsl.2011.09.038

Harmon, N., Rychert, C. A., Kendall, J. M., Agius, M., Bogiatzis, P., & Tharimena, S. (2020). Evolution of the oceanic lithosphere in the equatorial Atlantic from Rayleigh wave tomography, evidence for small-scale convection from the PI-LAB experiment. *Geochemistry, Geophysics, Geosystems*, *21*(9), e2020GC009174. https://doi.org/10.1029/2020GC009174

Hasterok, D. (2010). *Thermal state of continental and oceanic lithosphere*. The University of Utah.

Hasterok, D., Chapman, D., & Davis, E. (2011). Oceanic heat flow: Implications for global heat loss. *Earth and Planetary Science Letters*, *311*(3–4), 386–395. https://doi.org/10.1016/j.epsl.2011.09.044

Havlin, C., Chavan, K., Holtzman, B., Russell, J., Hariharan, A., Hopper, E., et al. (2025). vbr-calc/vbr: Release v1.2.1. *Zenodo*. https://doi.org/10.5281/zenodo.14674537

Havlin, C., Holtzman, B. K., & Hopper, E. (2021). Inference of thermodynamic state in the asthenosphere from anelastic properties, with applications to North American upper mantle. *Physics of the Earth and Planetary Interiors*, *314*, 106639. https://doi.org/10.1016/j.pepi.2020.106639

Haxby, W. F., & Weissel, J. K. (1986). Evidence for small-scale mantle convection from Seasat altimeter data. *Journal of Geophysical Research*, *91*(B3), 3507–3520. https://doi.org/10.1029/JB091iB03p03507

Heister, T., Dannberg, J., Gassmöller, R., & Bangerth, W. (2017). High accuracy mantle convection simulation through modern numerical methods–II: Realistic models and problems. *Geophysical Journal International*, *210*(2), 833–851. https://doi.org/10.1093/gji/ggx195

Herrmann, R. B. (2013). Computer programs in seismology: An evolving tool for instruction and research. *Seismological Research Letters*, *84*(6), 1081–1088. https://doi.org/10.1785/0220110096

Hillier, J., & Watts, A. (2005). Relationship between depth and age in the North Pacific Ocean. *Journal of Geophysical Research*, *110*(B2), B02405. https://doi.org/10.1029/2004jb003406

Hirschmann, M. M. (2006). Water, melting, and the deep Earth H_2O cycle. *Annual Review of Earth and Planetary Sciences*, *34*(1), 629–653. https://doi.org/10.1146/annurev.earth.34.031405.125211

Hirth, G., & Kohlstedt, D. L. (1996). Water in the oceanic upper mantle: Implications for rheology, melt extraction and the evolution of the lithosphere. *Earth and Planetary Science Letters*, *144*(1–2), 93–108. https://doi.org/10.1016/0012-821X(96)00154-9

Hirth, G., & Kohlstedt, D. L. (2003). Rheology of the upper mantle and the mantle wedge: A view from the experimentalists. *Geophysical Monograph Series*, *138*, 83–106. (Publisher: AGU AMERICAN GEOPHYSICAL UNION).

Hofmeister, A. (1999). Mantle values of thermal conductivity and the geotherm from phonon lifetimes. *Science*, *283*(5408), 1699–1706. https://doi.org/10.1126/science.283.5408.1699

Honda, S., & Yuen, D. (2001). Interplay of variable thermal conductivity and expansivity on the thermal structure of oceanic lithosphere. *Geophysical Research Letters*, *28*(2), 351–354. https://doi.org/10.1029/2000gl012096

Hua, J., Fischer, K. M., Becker, T. W., Gazel, E., & Hirth, G. (2023). Asthenospheric low-velocity zone consistent with globally prevalent partial melting. *Nature Geoscience*, *16*(2), 175–181. https://doi.org/10.1038/s41561-022-01116-9

Huang, J., & Zhong, S. (2005). Sublithospheric small-scale convection and its implications for the residual topography at old ocean basins and the plate model. *Journal of Geophysical Research*, *110*(B5), B05404. https://doi.org/10.1029/2004jb003153

Huang, J., Zhong, S., & Van Hunen, J. (2003). Controls on sublithospheric small-scale convection. *Journal of Geophysical Research*, *108*(B8), 2003JB002456. https://doi.org/10.1029/2003JB002456

Jarvis, G. T., & Mckenzie, D. P. (1980). Convection in a compressible fluid with infinite Prandtl number. *Journal of Fluid Mechanics*, *96*(3), 515–583. https://doi.org/10.1017/s002211208000225x

Kang, H., Kim, Y., Hung, S., Lin, P. P., Isse, T., Kawakatsu, H., et al. (2023). Seismic velocity structure of upper mantle beneath the oldest Pacific seafloor: Insights from finite-frequency tomography. *Geochemistry, Geophysics, Geosystems*, *24*(9), e2022GC010833. https://doi.org/10.1029/2022GC010833

Kang, L., & Karato, S.-I. (2023). Hydrogen Partitioning between Olivine and Orthopyroxene: Implications for the lithosphere-asthenosphere Structure. *Journal of Geophysical Research: Solid Earth*, *128*(2), e2022JB025259. https://doi.org/10.1029/2022JB025259

Kawano, Y., Isse, T., Takeo, A., Kawakatsu, H., Morishige, M., Shiobara, H., et al. (2023). Seismic structure of the lithosphere-asthenosphere system beneath the oldest seafloor revealed by Rayleigh-wave dispersion analysis. *Journal of Geophysical Research: Solid Earth*, *128*(6), 1–17. https://doi.org/10.1029/2023JB026529

Koppers, A. A. P., Staudigel, H., Pringle, M. S., & Wijbrans, J. R. (2003). Short-lived and discontinuous intraplate volcanism in the South Pacific: Hot spots or extensional volcanism? *Geochemistry, Geophysics, Geosystems*, *4*(10), 1089. https://doi.org/10.1029/2003GC000533

Korenaga, J., & Jordan, T. H. (2002). Onset of convection with temperature-and depth-dependent viscosity. *Geophysical Research Letters*, *29*(19), 29-1–29-4. https://doi.org/10.1029/2002gl015672

Korenaga, J., & Jordan, T. H. (2003a). Linear stability analysis of Richter rolls. *Geophysical Research Letters*, *30*(22), 2157. https://doi.org/10.1029/2003gl018337

Korenaga, J., & Jordan, T. H. (2003b). Physics of multiscale convection in Earth's mantle: Onset of sublithospheric convection. *Journal of Geophysical Research*, *108*(B7), 2333. https://doi.org/10.1029/2002jb001760

Korenaga, J., & Jordan, T. H. (2004). Physics of multiscale convection in Earth's mantle: Evolution of sublithospheric convection. *Journal of Geophysical Research*, *109*(B1), B01405. https://doi.org/10.1029/2003jb002464

Korenaga, T., & Korenaga, J. (2008). Subsidence of normal oceanic lithosphere, apparent thermal expansivity, and seafloor flattening. *Earth and Planetary Science Letters*, *268*(1–2), 41–51. https://doi.org/10.1016/j.epsl.2007.12.022

Kronbichler, M., Heister, T., & Bangerth, W. (2012). High accuracy mantle convection simulation through modern numerical methods. *Geophysical Journal International*, *191*(1), 12–29. https://doi.org/10.1111/j.1365-246x.2012.05609.x

Lei, W., Ruan, Y., Bozdağ, E., Peter, D., Lefebvre, M., Komatitsch, D., et al. (2020). Global adjoint tomography—Model GLAD-M25. *Geophysical Journal International*, *223*(1), 1–21. https://doi.org/10.1093/gji/ggaa253

Likerman, J., Zlotnik, S., & Li, C.-F. (2021). The effects of small-scale convection in the shallow lithosphere of the North Atlantic. *Geophysical Journal International*, *227*(3), 1512–1522. https://doi.org/10.1093/gji/ggab286

Lin, P.-Y. P., Gaherty, J. B., Jin, G., Collins, J. A., Lizarralde, D., Evans, R. L., & Hirth, G. (2016). High-resolution seismic constraints on flow dynamics in the oceanic asthenosphere. *Nature*, *535*(7613), 538–541. https://doi.org/10.1038/nature18012

Ma, Z., & Dalton, C. A. (2019). Evidence for dehydration-modulated small-scale convection in the oceanic upper mantle from seafloor bathymetry and Rayleigh wave phase velocity. *Earth and Planetary Science Letters*, *510*, 12–25. https://doi.org/10.1016/j.epsl.2018.12.030

Macdonald, K. C., Sempere, J.-C., Fox, P. J., & Tyce, R. (1987). Tectonic evolution of ridge-axis discontinuities by the meeting, linking, or self-decapitation of neighboring ridge segments. *Geology*, *15*(11), 993. https://doi.org/10.1130/0091-7613(1987)15〈993:TEORDB〉2.0.CO;2

Marquart, G. (2001). On the geometry of mantle flow beneath drifting lithospheric plates. *Geophysical Journal International*, *144*(2), 356–372. https://doi.org/10.1046/j.0956-540x.2000.01325.x

Marquart, G., Schmeling, H., & Braun, A. (1999). Small-scale instabilities below the cooling oceanic lithosphere. *Geophysical Journal International*, *138*(3), 655–666. https://doi.org/10.1046/j.1365-246x.1999.00885.x

McKenzie, D., Jackson, J. A., & Priestley, K. (2005). Thermal structure of oceanic and continental lithosphere. *Earth and Planetary Science Letters*, *233*(3–4), 337–349. https://doi.org/10.1016/j.epsl.2005.02.005

Michael, P. J. (1988). The concentration, behavior and storage of H_2O in the suboceanic upper mantle: Implications for mantle metasomatism. *Geochimica et Cosmochimica Acta*, *52*(2), 555–566. https://doi.org/10.1016/0016-7037(88)90110-X

Montagner, J. P., & Nataf, H. C. (1986). A simple method for inverting the azimuthal anisotropy of surface waves. *Journal of Geophysical Research*, *91*(B1), 511–520. https://doi.org/10.1029/jb091ib01p00511

Morgan, J. P., & Morgan, W. J. (2024). H, He, and seismic evidence for a bilithologic plume-fed asthenosphere. https://doi.org/10.5194/egusphere-egu24-16479

Munch, F. D., Romanowicz, B., Mukhopadhyay, S., & Rudolph, M. L. (2024). Deep mantle plumes feeding periodic alignments of asthenospheric fingers beneath the central and southern Atlantic Ocean. *Proceedings of the National Academy of Sciences of the United States of America*, *121*(46), e2407543121. https://doi.org/10.1073/pnas.2407543121

Naif, S., Key, K., Constable, S., & Evans, R. L. (2013). Melt-rich channel observed at the lithosphere-asthenosphere boundary. *Nature*, *495*(7441), 356–359. https://doi.org/10.1038/nature11939

Nishimura, C. E., & Forsyth, D. W. (1989). The anisotropic structure of the upper mantle in the Pacific. *Geophysical Journal International*, *96*(2), 203–229. https://doi.org/10.1111/j.1365-246X.1989.tb04446.x

Olugboji, T. M., Karato, S., & Park, J. (2013). Structures of the oceanic lithosphere-asthenosphere boundary: Mineral-physics modeling and seismological signatures. *Geochemistry, Geophysics, Geosystems*, *14*(4), 880–901. https://doi.org/10.1002/ggge.20086

Panet, I., Greff-Lefftz, M., & Romanowicz, B. (2024). Partial melt in mesoscale upper mantle upwellings beneath ocean basins. *Earth and Planetary Science Letters*, *639*, 118763. https://doi.org/10.1016/j.epsl.2024.118763

Parmentier, E. (2015). The dynamics and convective evolution of the upper mantle. In *Treatise on geophysics* (pp. 319–337). Elsevier. https://doi.org/10.1016/B978-0-444-53802-4.00131-7

Parsons, B., & McKenzie, D. (1978). Mantle convection and the thermal structure of the plates. *Journal of Geophysical Research*, *83*(B9), 4485–4496. https://doi.org/10.1029/JB083iB09p04485

Parsons, B., & Sclater, J. G. (1977). An analysis of the variation of ocean floor bathymetry and heat flow with age. *Journal of Geophysical Research*, *82*(5), 803–827. https://doi.org/10.1029/jb082i005p00803

Phillips, J., Gaherty, J. B., Russell, J. B., Eilon, Z., Forsyth, D. W., & Byrnes, J. (2023). Spatial variation in anisotropic shear velocity of old oceanic lithosphere-asthenosphere in the Southwest Pacific. In *AGU Fall Meeting Abstracts* (Vol. 2023, p. DI42A-01).

Plank, T., & Langmuir, C. H. (1992). Effects of the melting regime on the composition of the oceanic crust. *Journal of Geophysical Research*, *97*(B13), 19749–19770. https://doi.org/10.1029/92JB01769

Raitt, R. W., Shor, G. G., Francis, T. J. G., & Morris, G. B. (1969). Anisotropy of the Pacific Upper Mantle. *Journal of Geophysical Research*, *74*(12), 3095–3109. https://doi.org/10.1029/jb074i012p03095

Ramirez, F. D., Conrad, C. P., & Selway, K. (2023). Grain size reduction by plug flow in the wet oceanic upper mantle explains the asthenosphere's low seismic Q zone. *Earth and Planetary Science Letters*, *616*, 118232. https://doi.org/10.1016/j.epsl.2023.118232

Richards, F. D., Hoggard, M. J., Cowton, L. R., & White, N. J. (2018). Reassessing the thermal structure of oceanic lithosphere with revised global inventories of basement depths and heat flow measurements. *Journal of Geophysical Research: Solid Earth*, *123*(10), 9136–9161. https://doi.org/10.1029/2018JB015998

Richter, F. M. (1973). Convection and the large-scale circulation of the mantle. *Journal of Geophysical Research*, *78*(35), 8735–8745. https://doi.org/10.1029/JB078i035p08735

Rozel, A., Ricard, Y., & Bercovici, D. (2011). A thermodynamically self-consistent damage equation for grain size evolution during dynamic recrystallization. *Geophysical Journal International*, *184*(2), 719–728. https://doi.org/10.1111/j.1365-246x.2010.04875.x

Russell, J. B. (2021). *Structure and evolution of the oceanic lithosphere-asthenosphere system from high-resolution surface-wave imaging* (PhD Thesis) (ISBN: 9798569998982 Publication Title: ProQuest Dissertations and Theses). Columbia University.

Russell, J. B., Dalton, C. A., Havlin, C., Holtzman, B. K., Eilon, Z., Gaherty, J. B., & Forsyth, D. W. (2023). A dynamic oceanic asthenosphere revealed by high shear attenuation in the Pacific. In *AGU Fall Meeting Abstracts* (Vol. 2023, p. DI13B-0032).

Russell, J. B., Gaherty, J. B., Lin, P. P., Lizarralde, D., Collins, J. A., Hirth, G., & Evans, R. L. (2019). High-resolution constraints on Pacific upper mantle petrofabric inferred from surface-wave anisotropy. *Journal of Geophysical Research: Solid Earth*, *124*(1), 631–657. https://doi.org/10.1029/2018JB016598

Russell, J. B., Gaherty, J. B., Mark, H. F., Hirth, G., Hansen, L. N., Lizarralde, D., et al. (2022). Seismological evidence for girdled olivine lattice-preferred orientation in oceanic lithosphere and implications for mantle deformation processes during seafloor spreading. *Geochemistry, Geophysics, Geosystems*, *23*(10), 1–22. https://doi.org/10.1029/2022GC010542

Schmandt, B., & Humphreys, E. (2010). Seismic heterogeneity and small-scale convection in the southern California upper mantle: Southern CA mantle V_p and V_s structure. *Geochemistry, Geophysics, Geosystems*, *11*(5), Q05004. https://doi.org/10.1029/2010GC003042

Schubert, G., Turcotte, D. L., & Olson, P. (2001). *Mantle convection in the Earth and planets*. Cambridge University Press.

Semple, A., & Lenardic, A. (2018). Plug flow in the Earth's asthenosphere. *Earth and Planetary Science Letters*, *496*, 29–36. https://doi.org/10.1016/j.epsl.2018.05.030

Semple, A., & Lenardic, A. (2020). The robustness of pressure-driven asthenospheric flow in mantle convection models with plate-like behavior. *Geophysical Research Letters*, *47*(17), 1–7. https://doi.org/10.1029/2020GL089556

Sleep, N. H. (2011). Small-scale convection beneath oceans and continents. *Chinese Science Bulletin*, *56*(13), 1292–1317. https://doi.org/10.1007/s11434-011-4435-x

Sparks, D. W., & Parmentier, E. M. (1993). The structure of three-dimensional convection beneath oceanic spreading centres. *Geophysical Journal International*, *112*(1), 81–91. https://doi.org/10.1111/j.1365-246X.1993.tb01438.x

Stein, C. A., & Stein, S. (1992). A model for the global variation in oceanic depth and heat flow with lithospheric age. *Nature*, *359*(6391), 123–129. https://doi.org/10.1038/359123a0

Stein, C. A., & Stein, S. (1993). Constraints on pacific midplate swells from global depth-age and heat flow-age models. In *The Mesozoic Pacific: Geology, Tectonics, and Volcanism*, *Geophysical Monograph Series* (Vol. 77, pp. 53–76).

Stern, T. A., Henrys, S. A., Okaya, D., Louie, J. N., Savage, M. K., Lamb, S., et al. (2015). A seismic reflection image for the base of a tectonic plate. *Nature*, *518*(7537), 85–88. https://doi.org/10.1038/nature14146

Stotz, I., Iaffaldano, G., & Davies, D. R. (2018). Pressure-driven Poiseuille flow: A major component of the torque-balance governing pacific plate motion. *Geophysical Research Letters*, *45*(1), 117–125. https://doi.org/10.1002/2017gl075697

Takei, Y. (2002). Effect of pore geometry on V_p and V_s: From equilibrium geometry to crack. *Journal of Geophysical Research*, *107*(B2), 2043. https://doi.org/10.1029/2001JB000522

Takei, Y. (2017). Effects of partial melting on seismic velocity and attenuation: A new insight from experiments. *Annual Review of Earth and Planetary Sciences*, *45*(1), 447–470. https://doi.org/10.1146/annurev-earth-063016-015820

Takeo, A., Forsyth, D. W., Weeraratne, D. S., & Nishida, K. (2014). Estimation of azimuthal anisotropy in the NW Pacific from seismic ambient noise in seafloor records. *Geophysical Journal International*, *199*(1), 11–22. https://doi.org/10.1093/gji/ggu240

Takeo, A., Kawakatsu, H., Isse, T., Nishida, K., Shiobara, H., Sugioka, H., et al. (2018). In situ characterization of the lithosphere-asthenosphere system beneath NW Pacific Ocean via broadband dispersion survey with two OBS arrays. *Geochemistry, Geophysics, Geosystems*, *19*(9), 3529–3539. https://doi.org/10.1029/2018GC007588

Takeo, A., Kawakatsu, H., Isse, T., Nishida, K., Sugioka, H., Ito, A., et al. (2016). Seismic azimuthal anisotropy in the oceanic lithosphere and asthenosphere from broadband surface wave analysis of OBS array records at 60 Ma seafloor. *Journal of Geophysical Research: Solid Earth*, *121*(3), 1927–1947. https://doi.org/10.1002/2015jb012429

Takeo, A., Nishida, K., Isse, T., Kawakatsu, H., Shiobara, H., Sugioka, H., & Kanazawa, T. (2013). Radially anisotropic structure beneath the Shikoku Basin from broadband surface wave analysis of ocean bottom seismometer records. *Journal of Geophysical Research: Solid Earth*, *118*(6), 2878–2892. https://doi.org/10.1002/jgrb.50219

Thrastarson, S., Van Herwaarden, D.-P., Noe, S., Josef Schiller, C., & Fichtner, A. (2024). REVEAL: A global full-waveform inversion model. *Bulletin of the Seismological Society of America*, *114*(3), 1392–1406. https://doi.org/10.1785/0120230273

van Hunen, J., & Čadek, O. (2009). Reduced oceanic seismic anisotropy by small-scale convection. *Earth and Planetary Science Letters*, *284*(3–4), 622–629. https://doi.org/10.1016/j.epsl.2009.05.034

van Hunen, J., Huang, J., & Zhong, S. (2003). The effect of shearing on the onset and vigor of small-scale convection in a Newtonian Rheology. *Geophysical Research Letters*, *30*(19), 1991. https://doi.org/10.1029/2003gl018101

Van Hunen, J., Zhong, S., Shapiro, N., & Ritzwoller, M. (2005). New evidence for dislocation creep from 3-D geodynamic modeling of the Pacific upper mantle structure. *Earth and Planetary Science Letters*, *238*(1–2), 146–155. https://doi.org/10.1016/j.epsl.2005.07.006

Weeraratne, D. S., Forsyth, D. W., Yang, Y., & Webb, S. C. (2007). Rayleigh wave tomography beneath intraplate volcanic ridges in the South Pacific. *Journal of Geophysical Research: Solid Earth*, *112*(B6), B06303. https://doi.org/10.1029/2006jb004403

Yabe, K., & Hiraga, T. (2020). Grain-boundary diffusion creep of olivine: 2. Solidus effects and consequences for the viscosity of the oceanic upper mantle. *Journal of Geophysical Research: Solid Earth*, *125*(8), 1–22. https://doi.org/10.1029/2020JB019416

Yabe, K., Sueyoshi, K., & Hiraga, T. (2020). Grain-boundary diffusion creep of olivine: 1. Experiments at 1 atm. *Journal of Geophysical Research: Solid Earth*, *125*(8), 1–33. https://doi.org/10.1029/2020JB019415

Yamauchi, H., & Takei, Y. (2016). Polycrystal anelasticity at near-solidus temperatures. *Journal of Geophysical Research: Solid Earth*, *121*(11), 7790–7820. https://doi.org/10.1002/2016JB013316

Yamauchi, H., & Takei, Y. (2024). Effect of melt on polycrystal anelasticity. *Journal of Geophysical Research: Solid Earth*, *129*(4), e2023JB027738. https://doi.org/10.1029/2023JB027738

Zhang, S., & Karato, S.-I. (1995). Lattice preferred orientation of olivine aggregates deformed in simple shear. *Nature*, *375*(6534), 774–777. https://doi.org/10.1038/375774a0